

Improved constraints on the Faraday rotation towards eight fast radio bursts using dense grids of polarized radio galaxies

AYUSH PANDHI ^{1,2} B. M. GAENSLER ^{3,1,2} ZIGGY PLEUNIS ^{4,5} SEBASTIAN HUTSCHENREUTER ⁶ CASEY LAW ^{7,8}
RYAN MCKINVEN ^{9,10} SHANE P. O’SULLIVAN ¹¹ EMILY B. PETROFF ¹² AND TESSA VERNSTROM ^{13,14}

- ¹David A. Dunlap Department of Astronomy and Astrophysics, University of Toronto, 50 St. George Street, Toronto, ON M5S 3H4, Canada
²Dunlap Institute for Astronomy and Astrophysics, University of Toronto, 50 St. George Street, Toronto, ON M5S 3H4, Canada
³Department of Astronomy and Astrophysics, 1156 High Street, University of California Santa Cruz, Santa Cruz, CA 95064, USA
⁴Anton Pannekoek Institute for Astronomy, University of Amsterdam, Science Park 904, 1098 XH Amsterdam, The Netherlands
⁵ASTRON, Netherlands Institute for Radio Astronomy, Oude Hoogeveensedijk 4, 7991 PD Dwingeloo, The Netherlands
⁶University of Vienna, Department of Astrophysics, Türkenschanzstrasse 17, 1180 Vienna, Austria
⁷Cahill Center for Astronomy and Astrophysics, MC 249-17 California Institute of Technology, Pasadena, CA 91125, USA
⁸Owens Valley Radio Observatory, California Institute of Technology, Big Pine, CA 93513, USA
⁹Department of Physics, McGill University, 3600 rue University, Montreal, QC H3A 2T8, Canada
¹⁰Trottier Space Institute, McGill University, 3550 rue University, Montreal, QC H3A 2A7, Canada
¹¹Departamento de Física de la Tierra y Astrofísica & IPARCOS-UCM, Universidad Complutense de Madrid, E-28040 Madrid, Spain
¹²Perimeter Institute for Theoretical Physics, 31 Caroline St., Waterloo, ON, N2L 2Y5, Canada
¹³CSIRO, Space and Astronomy, PO Box 1130, Bentley, WA 6102, Australia
¹⁴ICRAR, The University of Western Australia, 35 Stirling Hw, Crawley, WA 6009, Australia

ABSTRACT

We present 2–4 GHz observations of polarized radio galaxies towards eight fast radio bursts (FRBs), producing grids of Faraday rotation measure (RM) sources with sky densities of 9–28 polarized sources per square degree. Using a Bayesian interpolation framework, we constrain Galactic RM fluctuations below $\sim 1 \text{ deg}^2$ angular scales around the FRB positions. Despite the positions of all eight FRBs far from the Galactic plane, we constrain previously unresolved small-scale Galactic RM structures around six of the eight FRBs. In two of these fields, we find potential changes in the sign of the Galactic RM that are not captured by previous, sparsely sampled RM grid observations. Our Galactic RM estimate towards the FRBs differs between a few rad m^{-2} up to $\sim 40 \text{ rad m}^{-2}$ from the all-sky Galactic RM map of Hutschenreuter et al. (2022). Extrapolating our results to the known population of polarized FRB sources, we may be incorrectly interpreting the host galaxy RM for $\sim 30\%$ of the FRB source population with current RM grid observations. Measuring small-scale Galactic RM variations is crucial for identifying FRBs in low density and weakly magnetized environments, which in turn could serve as potent probes of cosmic magnetism. This framework of reconstructing continuous Galactic RM structure from RM grid observations can be readily applied to FRBs that fall in the sky coverage of upcoming large-sky radio polarization surveys of radio galaxies, such as the Very Large Array Sky Survey (VLASS) and the Polarization Sky Survey of the Universe’s Magnetism (POSSUM).

Keywords: Radio bursts (1339) — Milky Way magnetic fields (1057) — Polarimetry (1278)

1. INTRODUCTION

Fast radio bursts (FRBs) are millisecond-duration extragalactic radio transients that were discovered by Lorimer et al. (2007). To date, 802 FRB sources have

been reported¹ (e.g., the first Canadian Hydrogen Intensity Mapping Experiment FRB (CHIME/FRB) catalog; CHIME/FRB Collaboration et al. 2021) and just over ~ 100 of those sources have been associated with external galaxies (e.g., Bhandari et al. 2020a; Bhardwaj et al. 2024; Sharma et al. 2024; Shannon et al. 2024). FRBs have been observed to have a diverse set of local environments, including: in proximity to star forming regions (FRB 20180916B; Marcote et al. 2020), in a globular cluster (FRB 20200120E; Kirsten et al. 2022), and associated with compact, persistent radio sources (PRs) within dwarf galaxies (FRB 20121102A and FRB 20190520B; Chatterjee et al. 2017; Niu et al. 2022).

In addition, the magnetoionic properties of the local environment enshrouding the FRB source are encoded in the Faraday rotation incurred by the linearly polarized emission of the FRB as it propagates to Earth. As linearly polarized emission propagates through magnetoionic media, it undergoes a wavelength squared (λ^2)-dependent rotation of its intrinsic polarization position angle ψ_0 to the observed angle:

$$\psi(\lambda) = \psi_0 + \text{RM}\lambda^2. \quad (1)$$

The rotation measure (RM) depends on the integrated number density of electrons and parallel component of the magnetic field along the line of sight (LOS):

$$\text{RM} = 0.812 \int_z^0 \frac{n_e(z) B_{\parallel}(z)}{(1+z)^2} \frac{dl(z)}{dz} dz \text{ rad m}^{-2}. \quad (2)$$

In Equation 2, we integrate between the emitting source (at z) to the observer (at $z = 0$) such that the RM is positive when the average LOS magnetic field is pointed towards the observer and negative when it is pointed away from the observer. The electron density ($n_e(z)$) is in units of cm^{-3} , the LOS magnetic field strength ($B_{\parallel}(z)$) is in units of μG , and $dl(z)$ is the LoS line element at z in units of pc. Propagation through the same medium also causes a λ^2 dispersion of the radio emission, which is parameterized as the dispersion measure (DM):

$$\text{DM} = \int_0^z \frac{n_e(z)}{(1+z)} \frac{dl(z)}{dz} dz \text{ pc cm}^{-3}. \quad (3)$$

To precisely probe the local magnetoionic environment around the FRB, we need to account for, and subtract, contributions to the DM and RM from other, intervening, media along the LOS. We can express the observed

DM and RM (DM_{obs} and RM_{obs}) of an FRB in terms of the individual contributing components along the LOS:

$$\text{DM}_{\text{obs}} = \text{DM}_{\text{MW}} + \text{DM}_{\text{IGM}}(z) + \frac{\text{DM}_{\text{host}}}{(1+z)} \text{ pc cm}^{-3}; \quad (4)$$

$$\text{RM}_{\text{obs}} = \text{RM}_{\text{ion}} + \text{RM}_{\text{MW}} + \text{RM}_{\text{IGM}}(z) + \frac{\text{RM}_{\text{host}}}{(1+z)^2} \text{ rad m}^{-2}. \quad (5)$$

In Equations 4 and 5, the ‘‘MW’’ subscript denotes the Galactic DM or RM, which combines contributions from both the Milky Way (MW) disk and halo (DM_{disk} and DM_{halo} and RM_{disk} and RM_{halo}), the ‘‘IGM’’ subscript is the collective DM or RM contribution from the intergalactic medium (IGM), and the ‘‘host’’ subscript encompasses DM or RM contributions from the FRB local environment and host galaxy. In Equation 4, we have ignored the DM contribution from Earth’s ionosphere, which is typically only $\sim 10^{-5} \text{ pc cm}^{-3}$ (Lam et al. 2016) but we include the ionospheric RM contribution (RM_{ion}) in Equation 5, as RM_{ion} is generally on the order of $\sim 0.1 - 1 \text{ rad m}^{-2}$ (Sobey et al. 2019). To derive magnetoionic properties of FRB local environments and host galaxies, we are chiefly interested in obtaining DM_{host} and RM_{host} . Thus, our goal is to precisely account for, and subtract, all other foreground components in Equations 4 and 5.

In most cases, RM_{MW} is a significant contributor in Equation 5, and sometimes it can even be larger than the RM_{host} contribution. The best estimate of RM_{MW} over large areas of the sky is provided by Hutschenreuter et al. (2022, hereafter H22), who apply a Bayesian inference scheme on 55,190 RMs (mostly from radio galaxies; Van Eck et al. 2023), to reconstruct an all-sky interpolated map of RM_{MW} . However, there are two major limitations with the H22 RM_{MW} map: (i) the underlying RM data has an average density of only ~ 1 polarized source per square degree (mostly using the data of Taylor et al. 2009) and (ii) it has large statistical uncertainties (with typical uncertainties of $10 - 20 \text{ rad m}^{-2}$). Therefore, on average, RM variations on scales $\lesssim 1 \text{ deg}^2$ are unconstrained².

When looking at the local magnetoionic environments around FRBs, the large statistical uncertainty in RM_{MW} is propagated into our estimate for RM_{host} , which can make it difficult to, for example, identify FRBs originating from ‘‘clean’’ environments (i.e., with $\text{RM}_{\text{host}} \sim 0 \text{ rad m}^{-2}$). Identifying FRBs in these clean environments would provide evidence for FRB sources that lack dense circumburst material, which is a key prediction of

¹ Based on the FRB Newsletter Volume 05, Issue 11 published in November 2024.

² The sky density of RM sources is very inhomogeneous, so the exact scale of RM variations that is resolved varies over the sky.

many theories that invoke young neutron stars as FRB progenitors (e.g., Connor et al. 2016; Lyutikov et al. 2016; Metzger et al. 2017, 2019). Instead, these FRBs may indicate a population of sources that is older, where the circumburst environment has dissipated or the central engine has moved away from its point of origin over time. In addition, FRBs with $\text{RM}_{\text{host}} \sim 0 \text{ rad m}^{-2}$ can serve as direct probes of intergalactic magnetic fields and their evolution over cosmic time (e.g., see Ravi et al. 2016; Akahori et al. 2016).

Currently, the largest number of polarized FRB sources comes from the CHIME/FRB collaboration (including 128 non-repeating and 41 repeating FRBs Mckinven et al. 2023; Pandhi et al. 2024; Ng et al. 2024) and these FRBs have typical localization uncertainties of $\lesssim 1$ arcmin (CHIME/FRB Collaboration et al. 2024). Polarized FRBs detected using other telescopes often have even more precise sky positions than the CHIME/FRB sample, for example FRBs observed with the Deep Synoptic Array (with $\lesssim 2$ arcsec; Law et al. 2024) and the Australian Square Kilometer Array Pathfinder (with $\lesssim 1$ arcsec; Bannister et al. 2019; Bhandari et al. 2020b; Macquart et al. 2020; Shannon et al. 2024). The current state-of-the-art H22 RM_{MW} cannot accurately resolve RM variations on $\lesssim 1 \text{ deg}^2$ scales across the whole sky. For experiments requiring precise estimates of RM_{host} , such as studies of the magnetized IGM, we need higher density grids of polarized radio galaxies (i.e., RM grids) to probe RM variations on scales comparable to the FRB positional uncertainties.

In this paper, we aim to precisely constrain the Galactic RM towards eight FRBs, derive stronger constraints of their RM_{host} , and quantify the limitations imposed by the current H22 Galactic RM sky on our ability to identify FRBs from clean magnetoionic environments and use them as probes of cosmic magnetism. We present the results of two observing campaigns undertaken with the Karl G. Jansky Very Large Array (VLA) that detect RM grids of densities 9 – 28 polarized sources per square degree, each in a region centered on one of eight known FRB sky positions. We apply a similar Bayesian interpolation scheme to the one used by H22, but designed to be applied on discretized patches of the sky (Khadir et al. 2024), with which we reconstruct high resolution maps of RM_{MW} toward each FRB. We compare our results to those by H22 and discuss the small-scale RM fluctuations that we are now able to probe with higher density RM grids. Using these maps, we obtain an updated RM_{MW} towards each of the eight FRBs and more precisely constrain their local magnetoionic environments. We contextualize these results in light of upcoming large-sky polarization surveys and a

rapidly growing FRB catalog to highlight key science that will become possible within the next few years.

The remainder of this paper is structured as follows. In Section 2 we summarize the two VLA observing campaigns, the data reduction, and the compilation of RM grids. In Section 3, we break down the different DM and RM LOS components and our methodology of estimating each one. Results presenting the new RM_{MW} reconstructions and their impact on the FRB LOS RM decomposition are provided in Section 4. We discuss our results in Section 5 and identify key science questions that can be tackled with our methodology in the coming years.

2. DATA PROCESSING

The VLA is a radio telescope based in the Plains of San Agustin, New Mexico, and operated by the National Radio Astronomy Observatory (NRAO). The telescope is an array of 27 antennas; each antenna carries 10 receivers and is a 25-meter parabolic dish installed on an altitude-azimuth mount. The antennas are arranged into three elongated arms that each contain 9 antennas, allowing for a high degree of flexibility and control over baselines. The VLA has 4 standard configuration sizes: A, B, C, and D, which have longest baselines of 36.4, 11.4, 3.4, and 1.0 km, respectively.

2.1. 2018 VLA Observations

The first of two observing campaigns was conducted between February 22-27, 2018 (PI: Dr. Jamie Farnes) around FRB 20110523A (for more details about this FRB source, see Masui et al. 2015). These data were taken in the B-configuration at 2.0 – 4.0 GHz with 2 MHz channel spacing, 8-bit samplers, an integration time of 3 seconds and contain full polarization information. The observations have a Stokes I root-mean-square (rms) sensitivity of $\sim 30.7 \mu\text{Jy}/\text{beam}$ and the synthesized beamwidth is $2.1''$. The observation targeted ~ 90 known radio sources from the National Radio Astronomy Observatory VLA Sky Survey (NVSS; Condon et al. 1998) within a 1 deg radius of FRB 20110523A. Each radio source was observed for ~ 2.5 minutes, with the overall desired RM grid density of $\sim 25 \text{ sources deg}^{-2}$. The flux density scale, bandpass, delay, and polarization angle are calibrated using the bright radio source 3C286. The instrumental polarization leakage was calibrated with a known low polarization source, J1407+2827, and the complex gain calibrator was J2136+0041.

This general observing strategy was adopted and modified for follow-up RM grid observations around seven other FRBs in 2023, described in the next section.

2.2. 2023 VLA Observations

The second observing campaign (PI: Ayush Pandhi) was undertaken between February 18 and May 23, 2023 while the telescope was in its B-configuration. These radio continuum observations were also taken at 2.0 – 4.0 GHz with 2 MHz channel spacing, 8-bit samplers, an integration time of 3 seconds, an on source time of ~ 4 minutes per target, and we retain full polarization information. The Stokes I rms sensitivity is consistently $18.75 \mu\text{Jy}/\text{beam}$ across all observed fields and the synthesized beamwidth is $2.1''$. For these observations we target a total of 164 radio sources in seven fields around FRBs 20160102A, 20181030A, 20190117A, 20190213B, 20190608B, 20191108A, and 20200120E.

The average target RM grid density around each of the seven FRBs was ~ 25 polarized sources per square degree. Thus, the average separation between RM grid sources approximately corresponds to the width of the error circle of the poorest localized FRB in our sample, FRB 20160102A. The RM grids are comprised of radio sources that were identified in the VLA Sky Survey (VLASS; Lacy et al. 2020) quick look catalog (Gordon et al. 2021). VLASS is observed in the same frequency range (2.0 – 4.0 GHz) and has the same angular resolution ($2.1''$) as our VLA observations, though a complete polarization catalog from the survey has not yet been released. Selecting our RM grid sources from this catalog ensures that we are confident in the flux density of each radio source and know a-priori whether sources will be resolved or unresolved. From this catalog, we targeted all ≥ 3 mJy radio sources in a 0.5 degree radius around each FRB position. Since most of the radio sources that we target are within a few mJy in flux of our faintest source, we observe all targets for ~ 4 minutes. Importantly, we diverge from the observing strategy employed in 2018 by selecting fewer but brighter radio sources per target and increasing the time on source. This was done with the expectation that a higher fraction of targeted sources would yield sufficient linearly polarized signal to measure their RMs. We only conduct on-axis observations of these radio galaxies in order to avoid off-axis instrumental polarization effects, which can introduce $\sim 10\%$ RM uncertainties (Ma et al. 2019).

For each field, we observed the quasar 3C138 as our flux density scale, bandpass, delay, and polarization angle calibrator. The instrumental leakage terms were calibrated by observing 3C84 – a bright, low polarization ($< 1\%$) source. A complex gain calibrator near each target field was observed every ~ 12 minutes; for this calibration we used: J2248-3235 for FRB 20160102A, J1048+7143 for FRBs 20181030A and 20200120E, J2152+1734 for FRB 20190117A,

J1800+7828 for FRB 20190213B, J2246-1206 for FRB 20190608B, and J1037+3309 for FRB 20191108A.

2.2.1. FRB sample

Multiple criteria were considered during the selection of FRB fields for the 2023 VLA observing campaign. First, we want to select FRBs for which the RM_{MW} contribution dominates, or is comparable to, the RM_{host} , as these FRBs most benefit from our analysis. We enforce this criteria by requiring that the FRB must already have a measured RM_{obs} and it must be $|\text{RM}_{\text{obs}}| < 1000 \text{ rad m}^{-2}$ since $\text{RM}_{\text{MW}} \ll 1000 \text{ rad m}^{-2}$ except along specific sightlines through the Galactic plane. We avoid FRBs near the Galactic plane by requiring that they must have a Galactic latitude $|b| > 25 \text{ deg}$ to minimize the likelihood of sharp RM_{MW} gradients that may be difficult to model even with high density RM grids. Priority is given to FRBs with positional uncertainties smaller than the sky area sampled by the currently available all-sky RM grid of density ~ 1 polarized source per square degree. Ideally we want our RM grids to probe a comparable angular scale to the FRB positional uncertainty. Furthermore, FRBs with associated host galaxies and independently measured redshifts are also prioritized. This information allows us to measure the RM_{host} contribution in the rest frame of the FRB and estimate the average LOS magnetic field strength in the FRB host galaxy. Finally, we deliberately choose to include a mix of repeating and non-repeating FRBs as target fields to ensure diversity in our sample and to enable potential analysis comparing the two sub-populations. Note that the selection process for these FRB fields predates some of the recent FRB polarization catalogs (e.g., Sherman et al. 2024; Pandhi et al. 2024), and hence the candidate pool of FRBs that satisfied the aforementioned criteria at the time these observations were proposed was very limited. Based on these criteria, we selected seven FRBs around which we aimed to derive high density RM grids using targeted VLA observations.

The seven FRBs in the 2023 VLA observations, as well as FRB 20110523A from the 2018 observations, have properties listed in Table 1. In Figure 1 we show their sky positions, colored by their RM_{obs} , overlaid on the H22 RM_{MW} sky.

2.3. VLA data reduction

All eight fields were processed through the standard VLA calibration pipeline,³ which performs basic flagging and calibration in the Common Astronomy Software Applications (CASA) program (CASA Team et al.

³ Details about the pipeline are provided by the NRAO.

Table 1. Summary of observed properties of the eight FRB sources (with repeaters in bold face) discussed in this work.

TNS Name	Modified Julian Date ^a	J2000 Right Ascension	J2000 Declination	DM _{obs} (pc cm ⁻³)	RM _{obs} (rad m ⁻²)	z _{host}
FRB 20110523A ¹	55704.6	21h45m12s ^b	-00°09m37s ^b	623.30(6)	-186.1(1.4)	-
FRB 20160102A ^{2,3}	57389.4	22h38m49s (7.5')	30°10m50s (7.5')	2596.1(3)	-221(6.4)	-
FRB 20181030A ^{4,5}	58870.4	10h34m22s (30.6'')	73°45m14s (47'')	103.500(13)	36.39(29)	0.00385
	58870.4			103.504(11)	37.67(54)	
	58870.9			103.493(83)	37.08(51)	
FRB 20190117A ^{5,6}	58500.9	22h06m38s (13'')	17°22m06s (13'')	393.062(74)	74.30(68)	-
	59532.1			395.804(36)	76.31(40)	
FRB 20190213B ^{5,6}	58834.4	18h25m02s (20'')	81°24m05s (26'')	301.64(12)	-3.63(41)	-
	59055.2			301.38(22)	1.04(42)	
	59261.7			301.400(48)	1.06(52)	
	59314.0			301.720(64)	0.97(52)	
	59431.3			301.430(19)	-0.28(42)	
FRB 20190608B ^{7,8}	58643.0	22h16m05s (0.2'')	-07°53m54s (0.2'')	340.05(6)	353(2)	0.11778
FRB 20191108A ⁹	58795.8	01h33m47s (3.5') ^c	31°51m30s (3.5')	588.1(1)	474(3)	-
FRB 20200120E ^{10,11,12}	58868.4	09h57m54.69935s (1.2 mas)	68°49m00.8529s (1.3 mas)	87.782(3)	-29.8(5)	^d
	59182.6			87.812(4)	26.8(3)	
	59265.9			87.7527(3)	-21.9(13.1)	
	59265.9			87.7527(3)	-57.2(5.1)	
	59280.7			87.7527(3)	-37.1(4.2)	
	59280.8			87.7527(3)	-36.4(8.0)	

¹ Masui et al. (2015); ² Bhandari et al. (2018); ³ Caleb et al. (2018); ⁴ Bhardwaj et al. (2021a); ⁵ Mckinven et al. (2023);⁶ Michilli et al. (2023); ⁷ Day et al. (2020); ⁸ Chittidi et al. (2021); ⁹ Connor et al. (2020); ¹⁰ Bhardwaj et al. (2021b);¹¹ Kirsten et al. (2022); ¹² Nimmo et al. (2022)^a The reported time of arrival of each burst at the respective observing telescope.^b No positional uncertainties are reported.^c The localization uncertainty was presented for the semi-major and semi-minor axes, which do not correspond to the Right ascension and Declination uncertainties directly. To be conservative, we have presented the uncertainty on the semi-major axis as the uncertainty on both the Right ascension and Declination.^d This FRB source is associated with the M81 galaxy, which is at a distance of 3.6 Mpc.

2022). For each field, we performed additional manual processing in CASA for each 128 MHz spectral window separately. First, we applied Hanning smoothing across the band to mitigate any radio frequency interference (RFI) that was not initially flagged, removed antenna-shadowed data, and removed RFI outliers in the time-frequency space using the **TFCrop** algorithm (using the default 4σ and 3σ thresholds for the time and frequency axes, respectively). The model visibility amplitude and phases of our calibrators were set using existing models of standard calibrators or by the model generated by the VLA calibration pipeline. We performed an initial phase and bandpass calibration on a subset of the central channels to average over temporal variation in the phases. Using the bandpass calibrator, we then solved for the antenna-based delays relative to the reference

antenna and derive a bandpass solution. For the polarization calibration, we first solved for the residual delay between the two cross-hand polarization outputs using **3C138**, then calibrated the instrumental polarization using the unpolarized source **3C84**, and solved for the correct polarization position angle using the reference model of **3C138**. Finally, we derived the complex antenna gain corrections across our observation, setting the zero phase to that of the reference antenna, using the respective gain calibrator for each field. The full set of calibration solutions was applied to all observed sources and we used the **TFCrop** and **RFFlag** algorithms for one last stage of RFI cleaning.

To clean and image our data, we employed the **tclean** functionality of CASA using an adapted version of the **CLEAN** deconvolver (Högbom 1974). We defined the ref-

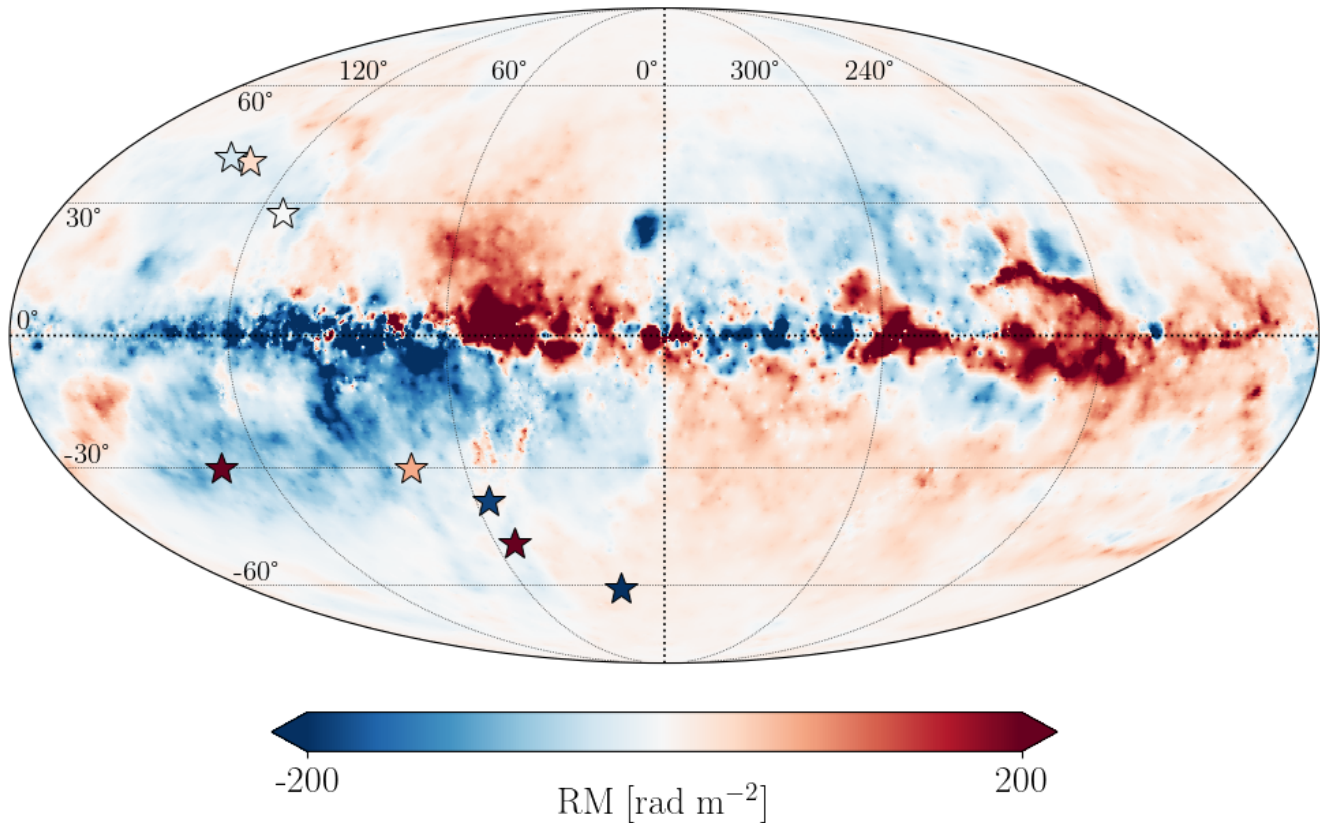


Figure 1. The eight targeted FRBs (stars) overlaid on the H22 reconstructed Galactic RM sky. Both the FRB markers and background map are colored based on their RM. For repeating FRBs, the mean RM across all bursts is used. The colorbar is saturated at $\pm 200 \text{ rad m}^{-2}$.

erence frequency to be 3.0 GHz, used two Taylor coefficients in the spectral model, applied a Briggs (1995) weighting scheme with the “robust” parameter set to 0.5, and set the maximum number of total iterations to 20,000 with a maximum number of minor-cycle iterations to be 1,000. For every observed radio source, we produced both a multi-frequency synthesis image (i.e., combining the signal over the observing frequency range to produce a single image) and Stokes I (total intensity), Q , U (orthogonal linear polarizations), and V (circular polarization) data cubes.

2.3.1. RM-synthesis

To estimate the RM of each radio source, we perform RM-synthesis (as implemented in the `RM-tools` package; Purcell et al. 2020) along the LOS corresponding to its brightest pixel. Note that the `RM-tools` implementation also accounts for the spectral index of the radio source by modeling the Stokes I spectrum and dividing it from the Stokes Q and U spectra. Here, we briefly summarize the RM-synthesis algorithm but for a more detailed description we refer the reader to the work by Burn (1966) and Brentjens & de Bruyn (2005). RM-synthesis relates the complex linearly polarized inten-

sity, $P(\lambda^2) = Q + iU$, to the Faraday dispersion function (FDF), $F(\phi)$, through a Fourier like transformation:

$$F(\phi) = \int_{-\infty}^{\infty} P(\lambda^2) e^{-2i\phi\lambda^2} d\lambda^2. \quad (6)$$

Here, ϕ is the Faraday depth and is a generalized form of the RM that accounts for multiple sources of Faraday rotation in the polarized emission along the LOS. In practice, RM-synthesis computes $F(\phi)$ for a range of trial values of ϕ to measure the total linearly polarized intensity across the observed spectrum at different Faraday depths. The limited bandwidth and sampling of the data means that the FDF is convolved with the rotation measure spread function (RMSF; Brentjens & de Bruyn 2005). The full width at half maximum (FWHM) of the RMSF, $\delta\phi$, effectively determines the resolution of the FDF in Faraday depth space as:

$$\delta\phi = \frac{3.79}{(\lambda_{\max}^2 - \lambda_{\min}^2)}, \quad (7)$$

for the maximum (λ_{\max}) and minimum (λ_{\min}) observed wavelength, respectively. For our observations between 2 – 4 GHz, we achieve $\delta\phi = 224.9 \text{ rad m}^{-2}$.

Faraday rotation contributed by an intervening screen appears as a delta function at $\phi = \text{RM}_{\text{obs}}$ convolved with the RMSF. Previous works have found that polarization properties derived with RM-synthesis may become unreliable for a polarized signal-to-noise ratio of $(\text{S/N})_P \leq 7$ (Brentjens & de Bruyn 2005; Macquart et al. 2012). Following the conservative approach used in a recent RM data release by the Polarization Sky Survey of the Universe’s Magnetism (POSSUM) collaboration (Vanderwoude et al. 2024), we consider a RM detection for a given radio source to be robust if it satisfies $(\text{S/N})_P = 8$. In this case, the ϕ value corresponding to the center of the peak in the FDF is the estimated RM. The measurement uncertainty on the RM_{obs} , $\delta(\text{RM}_{\text{obs}})$, is:

$$\delta(\text{RM}_{\text{obs}}) = \frac{\delta\phi}{2(\text{S/N})_P}. \quad (8)$$

2.3.2. Constructing the RM grids

After applying RM-synthesis to all observed radio sources, we can begin constructing the respective RM grids for each field. Keeping in mind that the purpose of these RM grids is to inform our view of RM_{MW} , we want to ensure that each radio source provides a clean probe of our Galaxy and, thus, we want to minimize contamination from other contributions along the LOS. We classify radio sources into three categories based on their FDF: (i) unpolarized, (ii) “Faraday simple”, or (iii) “Faraday complex”. In the foremost case, there is no $(\text{S/N})_P > 8$ peak in the FDF, so we are unable to sufficiently characterize its linear polarization properties and no RM estimate is derived. Unpolarized radio sources are removed from our sample and do not contribute to any RM grids. Faraday simple radio sources are those that have a singular peak in the FDF with $(\text{S/N})_P > 8$ at $\phi = \text{RM}$ and their RM uncertainty is computed following Equation 8. All Faraday simple sources are included in our RM grids. We note here that the determination of whether a linearly polarized radio source is Faraday simple or complex depends on whether we can resolve the different FDF components given our RMSF; hence, this determination depends on the frequency range of our observations. For example, a source that appears Faraday simple at high frequencies (due to a large RMSF that cannot resolve multiple, closely spaced FDF components) may actually be Faraday complex at low frequencies where the RMSF is smaller.

In some cases, the FDF of radio sources will have a $(\text{S/N})_P > 8$ detection but deviate from the single peak expected from a Faraday simple source. These sources are labelled “Faraday complex” and require careful handling if they are to be used in an RM grid to probe a foreground screen. Faraday complexity can manifest as

multiple FDF peaks or broadening of a FDF peak due to a variety of physical conditions, some examples include: multiple distinct RM contributing media along the LOS, unresolved RM components within the synthesized beam, an extended medium along the LOS that is both Faraday rotating and synchrotron emitting, or turbulence in a foreground magnetoionic screen on scales smaller than the projected size of the polarized source (for a more detailed description, see Vanderwoude et al. 2024). When dealing with multiple peaks in the FDF, it is difficult to ascribe a single RM value to the Faraday rotating screen that one is attempting to constrain. Meanwhile, for broadened FDF peaks, Equation 8 may not be an accurate description of the RM measurement uncertainty.

To quantify the extent of Faraday complexity present in a radio source’s FDF, we employ the M_2 metric developed by Brown (2011). First, we run the RM-CLEAN algorithm (Heald et al. 2009) to deconvolve the observed FDF with the RMSF and obtain a list of discrete ϕ values and their $|F(\phi)|$ amplitudes that exceed a signal-to-noise threshold of 8σ . We purposely choose 8σ to match our $(\text{S/N})_P > 8$ threshold following the setup used by Vanderwoude et al. (2024) to avoid over-cleaning the data. Using the RM-CLEAN products as inputs, we can then compute M_2 as the square root of the second moment of ϕ :

$$M_2 = \left[\frac{\sum_{i=1}^N (\phi_i - \bar{\phi})^2 |F(\phi_i)|}{\sum_{i=1}^N |F(\phi_i)|} \right]^{1/2}, \quad (9)$$

where the i subscript denotes each $> 8\sigma$ RM-CLEAN component for a total of N components and $\bar{\phi}$ is the first moment:

$$\bar{\phi} = \frac{\sum_{i=1}^N \phi_i |F(\phi_i)|}{\sum_{i=1}^N |F(\phi_i)|}. \quad (10)$$

To account for our effective resolution in $F(\phi)$ space, we normalize M_2 by $\delta\phi$,

$$m_2 = \frac{M_2}{\delta\phi}. \quad (11)$$

(Vanderwoude et al. 2024) and use m_2 as our final complexity metric.

For a Faraday simple source, with only one $> 8\sigma$ RM-CLEAN component, we would measure $m_2 = M_2 = 0$. As one adds more RM-CLEAN components, with increasing separation between them, and as their $|F(\phi)|$ amplitude becomes comparable to the primary FDF peak, m_2 increases. There are no strict rules regarding setting complexity thresholds for m_2 , so we determine two thresholds upon visual inspection of our data. First, we remove any radio sources with $m_2 > 0.25$ from our

sample, as these correspond to sources with multiple resolved peaks in their FDF such that we cannot unambiguously determine the Galactic RM along the LOS. We decide to include linearly polarized radio sources with $0.1 < m_2 < 0.25$, and with at least one secondary RM-CLEAN component that is $> 50\%$ of the $|F(\phi)|$ amplitude of the primary peak (i.e., two comparable, blended peaks), in our RM grids. Radio sources matching this criteria still have $\phi = \text{RM}$ but we update their RM uncertainty to be more conservative:

$$\delta(\text{RM}_{\text{obs,broad}}) = M_2. \quad (12)$$

All radio sources with $m_2 < 0.1$ are considered Faraday simple such that they depict only one FDF peak that is approximately Gaussian and are all included in our RM grids. A catalog of all RM sources used in this work is presented in Appendix A, which includes sky positions, RM and associated uncertainty, and m_2 .

3. FOREGROUND DM AND RM ESTIMATION

To derive magnetoionic properties of FRB local environments and host galaxies, we are chiefly interested in obtaining DM_{host} and RM_{host} . Thus, our goal is to precisely account for, and subtract, all other foreground components in Equations 4 and 5. In the following sections, we describe the methodology for estimating each of these foreground components.

3.1. Galactic and IGM DM contribution

To estimate the DM contribution from the FRB environment and host galaxy, DM_{host} , we need to estimate and subtract both the Galactic DM component (DM_{MW}) and, if possible, the IGM component (DM_{IGM}). Encompassed within the DM_{MW} term are both the DM contributions from the MW disk as well as from its halo. While multiple models of the Galactic disk DM contribution exist (e.g., Cordes & Lazio 2002; Hutschenreuter et al. 2024), we opt to use the thermal electron density n_e model of the Galactic disk by Cordes & Lazio (2002) (hereafter NE2001) as it is the most commonly used Galactic DM model for FRB studies and allows for direct comparison of our results to previous literature. We integrate through the full extent of the MW towards the best fit FRB position with the PyGEDM package (V3.1.1; Price et al. 2021) to obtain the DM contribution from the MW disk. For the MW halo, we assume a constant DM contribution as a function of sky position with a fiducial value of 30 pc cm^{-3} based on estimates by Dolag et al. (2015), Yamasaki & Totani (2020), and Cook et al. (2023). Further, if the FRB has been associated with a host galaxy that has a measured redshift, then the average $\text{DM}_{\text{IGM}}(z)$ along that

LOS can be calculated following the linear $\text{DM}_{\text{IGM}} - z$ relation (i.e., the ‘‘Macquart relation’’; Macquart et al. 2020). In this work, we use the $\text{DM}_{\text{IGM}} - z$ relation and its associated uncertainties as presented by Baptista et al. (2024).

3.2. Galactic RM contribution

The interpolation technique to constrain the Galactic RM component used in this work is based on Information Field Theory (IFT; Edenhofer et al. 2024), a Bayesian statistical framework to design non-parametric inference algorithms. The specialized application of an IFT algorithm for RM grids was first applied to all sky data sets by Oppermann et al. (2012, 2015), Hutschenreuter & Enßlin (2020), and recently H22. It has also been used to constrain the Galactic DM and LOS magnetic field skies (Pandhi et al. 2022; Hutschenreuter et al. 2024). For discrete sky patches, the RM interpolation method was tested by Khadir et al. (2024) and we refer the reader to this work for in-depth discussions of performance, possible biases, and comparisons to other techniques. Compared to the setup of Khadir et al. (2024), we have simplified the algorithm in that we only infer a single (Gaussian) field, instead of a product of an amplitude and sign field. This is owing to the relatively sparse sky sampling in some fields (i.e., ~ 9 polarized sources per square degree compared to the ~ 45 polarized sources per square degree used by Khadir et al. (2024), which makes a reduction of the parameter space necessary to stabilize the inference algorithm and avoid overfitting. The price for that is a reduced capability to represent strong variations (i.e., several orders of magnitude) in RM amplitude within a patch. Our model together with our choice of hyperparameters results in a marginal per pixel prior that allows RM amplitudes well over $\sim 100 \text{ rad m}^{-2}$. Since we are only reconstructing the RM_{MW} in small regions of the sky around FRBs at high Galactic latitude ($|b| > 25 \text{ deg}$), this range easily encompasses the expected amount of RM amplitude variations across our reconstruction area. Thus, we expect no meaningful impact of this modeling choice on the reconstructed RM_{MW} maps.

Another significant difference to the Khadir et al. (2024) implementation is that we included a noise estimation feature in the inference algorithm that automatically detects and down-weights extreme outliers in the data. This is useful for removing RM grid sources that are dominated by RM contributions local to the emitting source, and therefore are less suitable tracers of RM_{MW} . For details of this feature we refer the reader to Hutschenreuter & Enßlin (2020). The reliability of this outlier removal feature critically relies on number

statistics, i.e., the more data points constraining the MW component, the more likely we are able to correctly down-weight data points with a strong source contribution. For this reason, we have used RM data points from the catalog provided by Van Eck et al. (2023) in addition to the VLA observations when reconstructing maps of RM_{MW} . Given the relatively sparse sky sampling of these additional RMs, these mostly help to constrain the large angular scales (with respect to the field of view) around each FRB. We can test the impact of the VLA RMs by comparing our results to the all sky results of H22, which is constrained by the same catalog (see Section 4.2). We note that the additional RMs are largely of poorer quality compared to our VLA grid, as the catalog is dominated by RMs from the NVSS survey (Taylor et al. 2009), which were inferred from only two frequency bands. Possible problems resulting from this were discussed in detail by Ma et al. (2019), but Hutschenreuter & Enßlin (2020) demonstrated that the very same noise estimation feature as discussed above was able to reliably find and filter these problematic RMs. We have used sources from Van Eck et al. (2023) within a radius of three times the maximum extent of the respective VLA RM grid (i.e., within a 1.5 deg radius). We chose this limit, as sources further out will likely not be informative for the scales of the respective VLA field of view.

3.3. Ionospheric RM contribution

The ionospheric RM contribution depends on the LOS through the ionosphere, but also undergoes temporal variations related to the time of day and solar activity, so we need to measure RM_{ion} at the sky position and at time of arrival of each FRB. First, a magnetoionic model for the ionosphere is created by combining maps of the vertical total electron content in the ionosphere recorded using a distribution of Global Positioning System satellites with models of the Earth’s magnetic field at the time of arrival of an FRB. Then, an estimate of RM_{ion} is computed by integrating over the estimated trajectory of the FRB emission through the ionosphere. For this RM_{ion} estimation, we make use of the `RMextract` package of Mevius (2018).

4. RESULTS

4.1. RM grids

Following the steps laid out in Section 2.3.2, we construct RM grids for each of our eight VLA fields. In total, only 4 sources were omitted from our RM grids due to Faraday complexity ($m_2 > 0.25$). In Table 2 we describe the statistics for each RM grid including the number of observed sources in the field, num-

ber of RM grid sources per field, RM grid density, median RM_{obs} , median RM measurement uncertainty $\delta(\text{RM}_{\text{obs}})$, and a robust standard deviation of the RM_{obs} distribution calculated using the median absolute deviation from the median (MADFM) which approximates to $\sim 1.4826 \times \text{MADFM}$. Our RM grid density ranges between 9 and 28 sources per square degree. Note that a larger fraction of the observed radio sources in the FRB 20110523A field are unpolarized compared to the other seven fields because the 2018 VLA observing campaign selected fainter targets and spent less time observing each target compared to the 2023 observations. As a result, our RM grid density of the FRB 20110523A field is relatively low (9 sources deg^{-2}). All eight fields have a moderate median RM_{obs} magnitude on the order of 10 rad m^{-2} , as is generally expected for regions away from the Galactic plane (e.g., see Vanderwoude et al. 2024).

4.2. Reconstructed RM_{MW} maps

Using the Bayesian inference scheme described in Section 3.2, we derive reconstructed RM_{MW} and associated statistical uncertainty maps. The reconstructed RM_{MW} maps for each region are presented in the right-hand panels of Figures 2–3. For comparison, the H22 RM_{MW} maps are shown in the left-hand panels. The pixel scale for the H22 maps in a cartesian projection is 0.1435 deg and for the reconstructed RM_{MW} maps in this work it is 0.04 deg. In the center of each map, we show the respective FRB sky position as a star (with a black ellipse indicating its positional uncertainty) that is coloured by its RM_{obs} . In both the left- and right-hand panels, we overplot the previously existing extragalactic RM data in these regions from Van Eck et al. (2023) as squares. In the right-hand panels, we also plot the VLA RM grids derived in this work as circles and the unpolarized radio sources are shown as purple crosses. The aspect ratio of the plots depend on the Declination of the field (i.e., the vertical axis becomes more compact closer to Declination = ± 90 degrees). Notably, the FRB 20110523A field has a RM grid density > 1 source per square degree even prior to the inclusion of our VLA observations. This is because that region of the sky overlaps with the first data release of the Spectral and Polarisation in Cutouts of Extragalactic sources from The Rapid Australian Square Kilometer Array Pathfinder Continuum Survey (SPICE-RACS), which provides an average RM grid density of ~ 4 sources per square degree (Thomson et al. 2023). In Figures 4–5, we plot the associated RM statistical uncertainty maps from the Bayesian inference. Again, the H22 maps are on the left and those from our reconstruction are on the right and

Table 2. Summary of RM grid statistics for all eight VLA fields.

FRB Source	# of observed sources	# of RM grid sources	RM grid density (deg ⁻²)	Median RM _{obs} (rad m ⁻²)	Median δ (RM _{obs}) (rad m ⁻²)	RM _{obs} MADFM standard deviation (rad m ⁻²)
FRB 20110523A	35	7	9	13.7	7.3	10.5
FRB 20160102A	25	15	19	23.1	6.4	16.9
FRB 20181030A	24	8	10	-23.2	17.7	12.0
FRB 20190117A	24	16	20	-38.5	9.1	16.7
FRB 20190213B	19	12	15	10.7	7.4	18.8
FRB 20190608B	17	10	13	-22.7	8.2	15.3
FRB 20191108A	18	9	11	-64.1	10.7	32.7
FRB 20200120E	37	22	28	-17.1	5.6	21.0

the FRB position, and associated positional uncertainty, are plotted as a star and black ellipse, respectively. We note that the error maps, in parts, have different degrees of smoothness than the RM_{MW} maps. This reflects the very heterogeneous structure of the RM grids, both with respect to spatial structure as well as measurement uncertainty on the individual RM_{obs} measurements. This leads to varying degrees of certainty of our reconstruction within a given field, even if the posterior mean appears to be smoothly varying. In Figures 2–3, six out of eight of our reconstructed RM_{MW} maps show RM variations on $\lesssim 1$ deg² scales that were previously unresolved by the H22 all-sky reconstruction, or provide a more granular picture of larger scale RM variations. Only the field around FRBs 20181030A does not show any clear RM variations across the map, while around FRB 20190117A we recover a similar large scale RM gradient as seen in the H22 map. Even in fields without drastic small-scale RM variations, our reconstruction is still notably different from the H22 map, suggesting that we are also able to better constrain the large-scale RM variations with the addition of our localized, high-density RM grids. Qualitatively, in five of eight fields (FRBs 20110523A, 20160102A, 20190213B, 20190608B, and 20191108A), we uncover sharp small-scale variations in RM_{MW} (approximately $\sim 20 - 40$ rad m⁻² variations over $\sim 0.3 - 1$ deg scales). In the FRB 20200120E field we discover a previously unseen large-scale RM gradient that shows a change of ~ 30 rad m⁻² over ~ 3 deg. In all of these cases, the range of RM_{MW} values in our reconstruction is broader than the H22 map. For example, the H22 map shows a constant ~ 15 rad m⁻² across the FRB 20160102A field, while the RM_{MW} values in our reconstruction range over $\sim 9 - 35$ rad m⁻². In two maps (corresponding to FRBs 20110523A and 20190213B), we find changes in the RM sign that potentially suggest a flip in the average LOS magnetic field orientation across

the sky. We caution that in both of these fields, the RM sign flips appear to be driven largely by one RM source and, therefore, could instead be RM contribution intrinsic to the source. Furthermore, the negative RM regions in these two maps have RM_{MW} amplitudes close to 0 rad m⁻², which are comparable to or smaller than the RM_{MW} uncertainties in these areas, meaning that they may still be consistent with there being no physical RM sign flips.

Furthermore, as is clear in Figures 4–5, we reduce the average statistical uncertainty on RM_{MW} in all eight regions. The second panel of Figure 7 also shows that the RM_{MW} uncertainty at the position of all eight FRBs is lower in our reconstruction than in H22. Note that in the case of FRB 20190608B, the statistical RM_{MW} uncertainty in the north-eastern area is not constrained due to a lack of RM data points in that part of the sky. The reason that this issue only manifests in our reconstruction, and not in the H22 map, is because our inference model is computed only over a small region rather than over the entire sky.

4.3. FRB magnetoionic environments

In the top panel of Figure 6, we compare the RM_{MW} specifically towards each of the eight FRBs as determined by H22 (x-axis) and by our RM reconstruction (y-axis). For five of the eight FRBs, the RM_{MW} between the two reconstructions is consistent within statistical uncertainties. In the other three cases, the RM_{MW} between reconstructions is inconsistent, with the largest difference being 26 ± 13 rad m⁻² for FRB 20191108A. We compare the statistical uncertainties on RM_{MW} between the two reconstructions in the bottom panel of Figure 6. In all cases, the uncertainty is improved by a factor of 2–6 with our updated RM_{MW} reconstruction.

When redshift information for the FRB host galaxy is known, we derive its DM_{host} and RM_{host} following

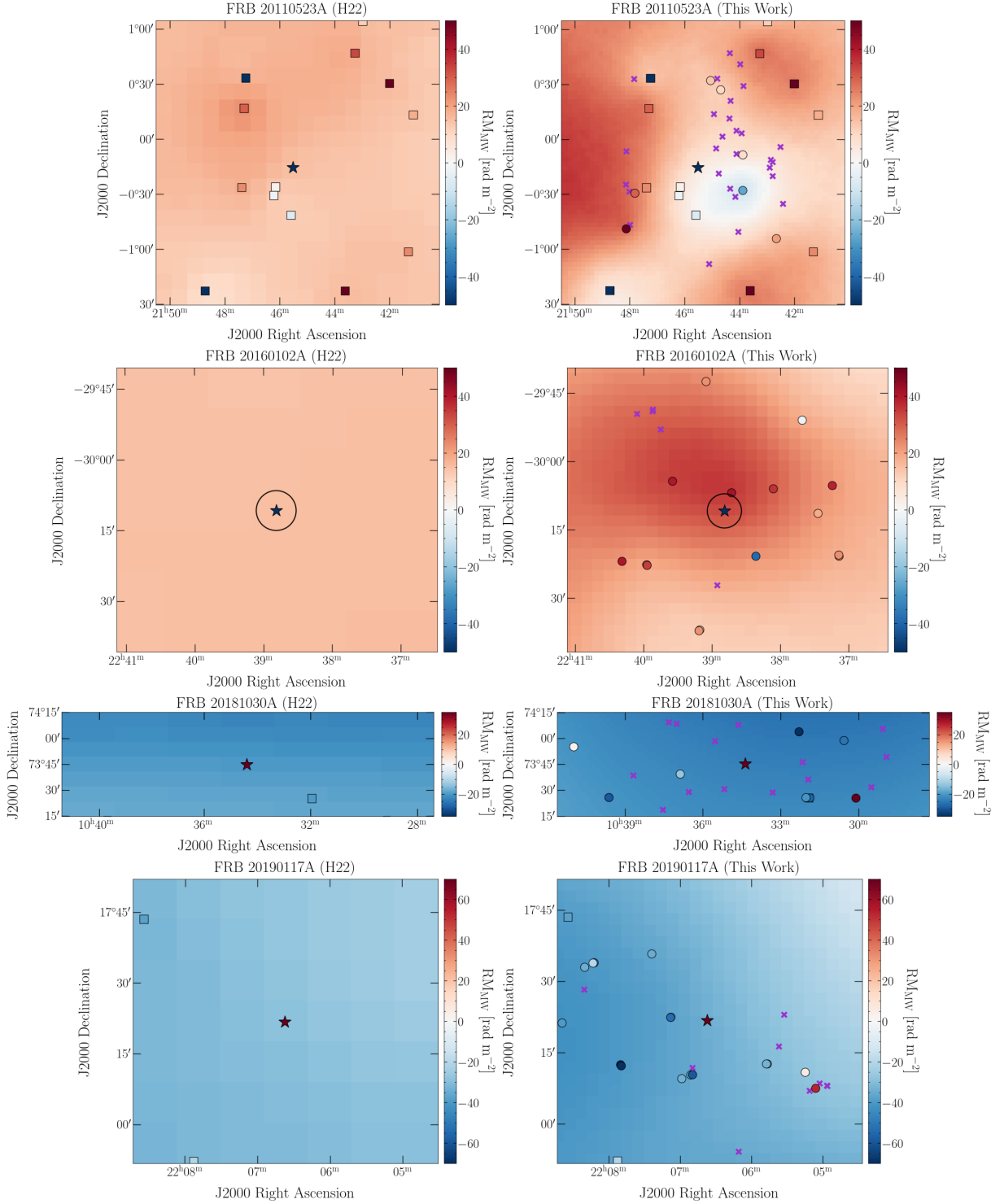


Figure 2. Comparison of the H22 RM_{MW} maps (left) and those reconstructed in this work (right) for FRBs 20110523A, 20160102A, 20181030A, and 20190117A, in order from top to bottom. Each FRB is presented by a star with a black ellipse representing its position uncertainty (in most cases the position uncertainty is smaller than the symbol). RMs of polarized radio galaxies observed prior to this work are shown as squares in both panels and our VLA RM grid sources (Faraday simple sources or those with $0.1 < m_2 < 0.25$) are shown as circles in the right panels. Sources that were observed but did not meet our linear polarization threshold of $(S/N)_P > 8$ are plotted as purple crosses in the right panels. The few Faraday complex sources with $m_2 > 0.25$ are not plotted. The background maps, FRBs, and polarized radio galaxies are all colored by their RM_{obs} . The aspect ratio of each panel depends on the Declination of the field (i.e., more compact closer to Declination = ± 90 degrees).

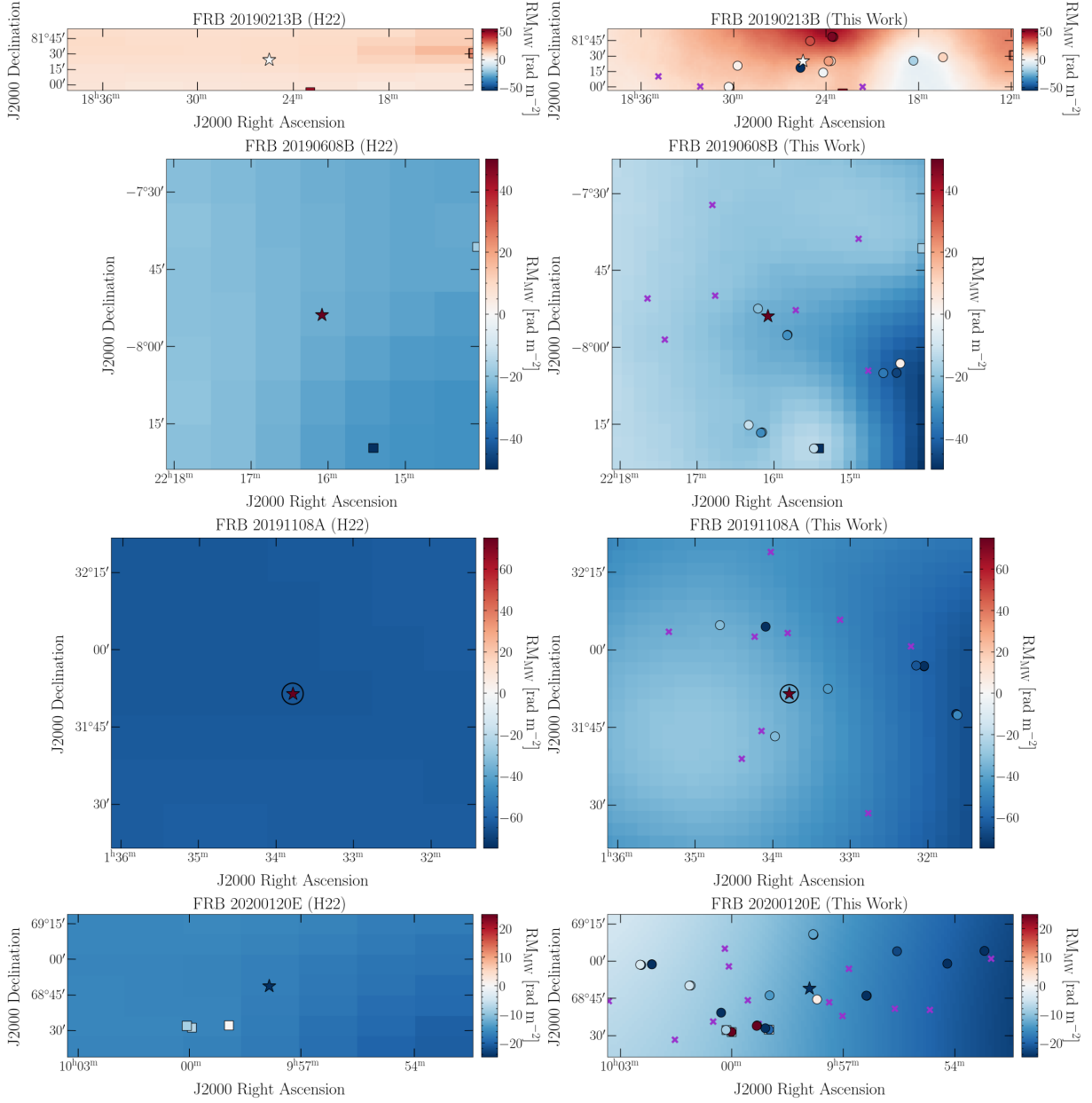


Figure 3. As for Figure 2 but for FRBs 20190213B, 20190608B, 20191108A, and 20200120E.

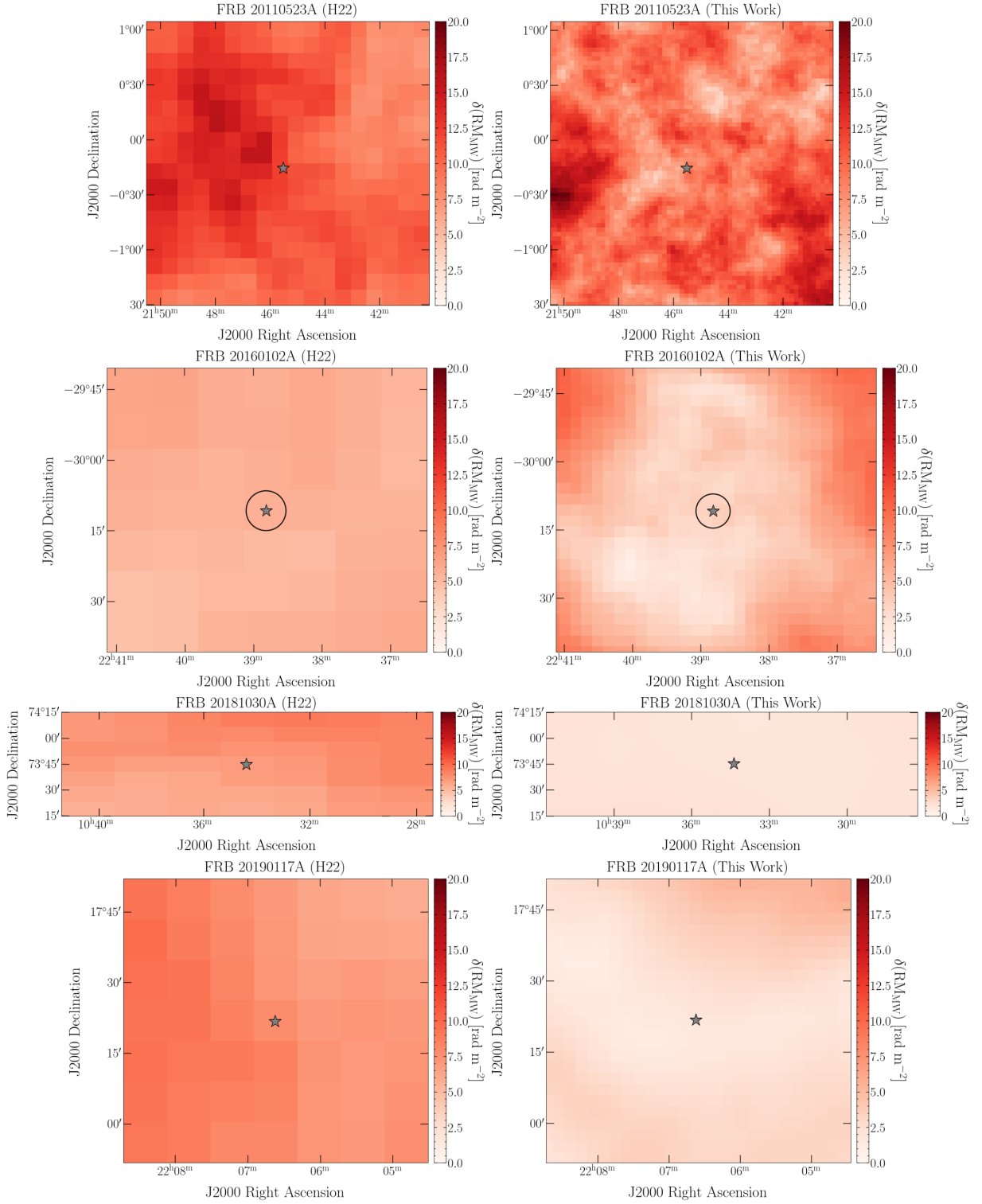


Figure 4. Comparison of the RM_{MW} uncertainty maps from H22 (left) and from this work (right) for FRBs 20110523A, 20160102A, 20181030A, and 20190117A (in order from top to bottom). The position of each FRB is plotted as grey star and their position uncertainty is plotted as black ellipse. In most cases, the position uncertainty is smaller than the symbol.

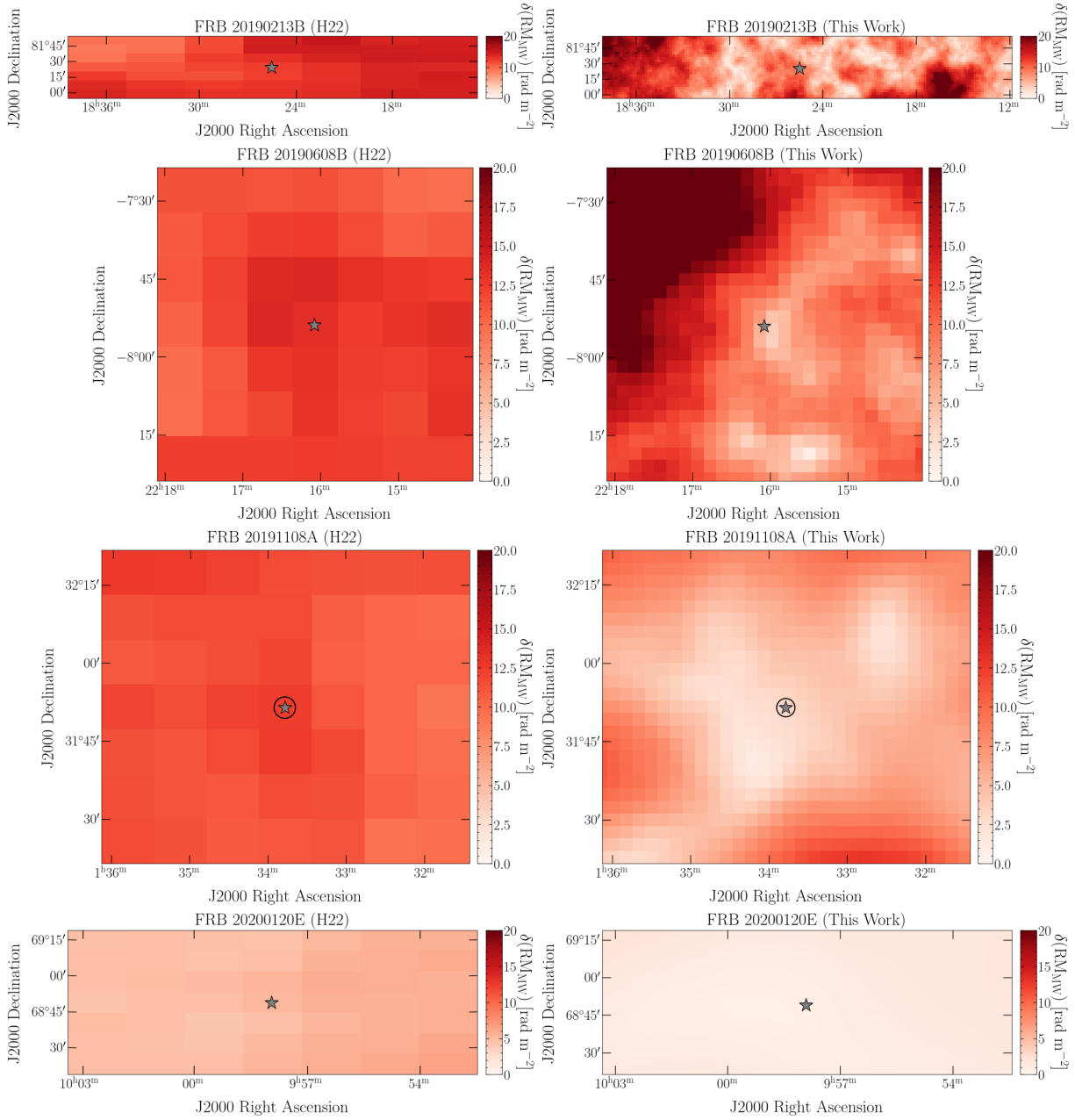


Figure 5. As for Figure 4 but for FRBs 20190213B, 20190608B, 20191108A, and 20200120E

Equations 4 and 5, respectively. Using these values, we can calculate the electron density-weighted average magnetic field strength parallel to the LOS in the FRB host galaxy as:

$$\langle B_{\parallel, \text{host}} \rangle = 1.232 \frac{\text{RM}_{\text{host}}}{\text{DM}_{\text{host}}} \mu\text{G}. \quad (13)$$

If the redshift of the FRB host galaxy is unknown, we instead compute the observer frame values:

$$\text{DM}_{\text{EG}} = \text{DM}_{\text{obs}} - \text{DM}_{\text{MW}} \text{ pc cm}^{-3}; \quad (14)$$

$$\text{RM}_{\text{EG}} = \text{RM}_{\text{obs}} - \text{RM}_{\text{MW}} \text{ rad m}^{-2}. \quad (15)$$

Here the subscript ‘‘EG’’ denotes the combined extragalactic contribution from the IGM and host galaxy in the observer frame. Then, the observer frame analog of $\langle B_{\parallel, \text{host}} \rangle$ is:

$$\beta = 1.232 \frac{\text{RM}_{\text{EG}}}{\text{DM}_{\text{EG}}} \mu\text{G}. \quad (16)$$

The uncertainties in some of our foreground estimates are strongly non-Gaussian and asymmetric. Below, we list the distributions and associated uncertainties for every foreground estimate in our DM and RM decomposition:

1. DM_{obs} : Drawn from a Gaussian distribution with mean equal to the measured DM_{obs} and the standard deviation equal to the associated measurement uncertainty. We note here that a Gaussian distribution is not always a reliable assumption for modeling DM_{obs} , which is a definite positive quantity, as it could lead to randomly drawn samples with negative DM_{obs} . In our case, the combination of relatively large DM_{obs} for our FRBs ($\gtrsim 88 \text{ pc cm}^{-3}$) and minuscule measurement uncertainties ($\lesssim 0.3 \text{ pc cm}^{-3}$) means that there is an extremely small likelihood of drawing a negative DM_{obs} . Therefore, the choice of a Gaussian distribution for DM_{obs} does not effect our results. However, we caution against the use of this assumption in cases where DM_{obs} is very small and/or the associated measurement uncertainty is large.
2. DM_{disk} : Drawn from a Uniform distribution with 20% uncertainties about the NE2001 prediction at the given sky position (Cordes & Lazio 2002).
3. DM_{halo} : We assumed 0.2 dex uncertainty about the fiducial 30 pc cm^{-3} used in this work (i.e., a Log-Normal distribution with mean $\ln(30)$ and variance $\ln(10^{0.2})$; Yamasaki & Totani 2020).
4. DM_{IGM} : Directly sampled from the probability distribution presented in Equation 1 by Baptista

et al. (2024). The DM_{IGM} is only included in the DM decomposition if the FRB has a known redshift.

5. RM_{obs} : Drawn from a Gaussian distribution with mean equal to the measured RM_{obs} and the standard deviation equal to the associated measurement uncertainty.
6. RM_{ion} : We use the estimate obtained from **RMextract** (Mevius 2018) without an associated uncertainty since RM_{ion} is much smaller than the other RM contributions along the LOS.
7. RM_{IGM} : Drawn from a Gaussian distribution with mean 0 rad m^{-2} and standard deviation 6 rad m^{-2} following Schnitzeler (2010).
8. RM_{MW} : Both estimate and associated uncertainty obtained from either the H22 maps or the reconstructed maps derived in this work.

Thus, we compute uncertainties on our estimates of DM_{host} , RM_{host} , and $\langle B_{\parallel, \text{host}} \rangle$ (or DM_{EG} , RM_{EG} , and β) using Monte Carlo random sampling. In this procedure, we randomly draw values for all foreground DM and RM components from their known underlying distributions, use those to compute DM_{host} , RM_{host} , and $\langle B_{\parallel, \text{host}} \rangle$ (or DM_{EG} , RM_{EG} , and β), and we repeat this process for 10,000 trials. We approximate our uncertainties as the 68% confidence interval around the median from the resulting DM_{host} , RM_{host} , and $\langle B_{\parallel, \text{host}} \rangle$ (or DM_{EG} , RM_{EG} , and β) distributions. In the second section of Table 3, we tabulate the DM_{host} , RM_{host} , and $\langle B_{\parallel, \text{host}} \rangle$ (or DM_{EG} , RM_{EG} , and β) of each FRB, computed using the H22 map and using our updated reconstruction. We quantify the impact of the updated RM_{MW} reconstruction on our understanding of the FRB magnetoionic environments in Figure 7. Specifically, we compare the magnitude of RM_{host} (or RM_{EG}) predicted by both reconstructions for each FRB.

4.4. The extragalactic RM contribution at 3 GHz

Previous RM surveys have been conducted primarily at or below 1.4 GHz (e.g., Taylor et al. 2009; O’Sullivan et al. 2023). In these studies, a model of the Galactic RM is subtracted from the RMs of the polarized radio galaxies themselves to obtain the sum of the extragalactic RM contributions along that LOS, RM_{EG} . We expect to see non-zero variance in the RM_{EG} distribution arising from differing intrinsic source environments, path lengths through the IGM, and intervening structures. At 144 MHz, $\sigma(\text{RM}_{\text{EG}})$ has been measured to be $1.8 - 4.0 \text{ rad m}^{-2}$ (O’Sullivan et al.

Table 3. Summary of DM and RM decomposition for each of the eight FRBs.

Foreground contributions					
FRB Source	DM _{MW} (pc cm ⁻³)	DM _{IGM} (pc cm ⁻³)	RM _{ion} (rad m ⁻²)	RM _{MW} (H22) (rad m ⁻²)	RM _{MW} (This work) (rad m ⁻²)
FRB 20110523A	73.4 ^{+17.6} _{-12.1}	–	2.4	14.9 ± 12.6	7.5 ± 6.7
FRB 20160102A	64.5 ^{+17.7} _{-11.8}	–	–2.0	14.9 ± 5.5	34.5 ± 3.7
FRB 20181030A	71.1 ^{+17.4} _{-12.3}	3.2 ^{+1.7} _{-1.0}	0.24	–19.6 ± 6.9	–23.8 ± 1.8
			0.23		
			0.51		
FRB 20190117A	78.2 ^{+17.6} _{-12.5}	–	0.84	–28.3 ± 7.4	–33.9 ± 1.9
			0.44		
FRB 20190213B	82.7 ^{+18.0} _{-13.0}	–	0.11	10.2 ± 12.2	23.1 ± 10.0
			0.34		
			0.69		
			0.54		
			0.38		
FRB 20190608B	67.3 ^{+17.7} _{-12.2}	99.9 ^{+46.5} _{-26.6}	–0.52	–24.4 ± 13.3	–22.7 ± 5.2
FRB 20191108A	81.8 ^{+18.3} _{-12.9}	–	0.23	–63.4 ± 12.4	–37.5 ± 3.0
FRB 20200120E	70.7 ^{+18.0} _{-12.3}	1.0 [†]	0.14	–17.0 ± 5.3	–13.6 ± 0.9
			0.34		
			0.20		
			0.20		
			0.41		
			0.39		
FRB Magnetoionic Environment					
FRB Source	DM _{host} (pc cm ⁻³)	RM _{host} (H22) (rad m ⁻²)	RM _{host} (This work) (rad m ⁻²)	B _{host} (H22) (μG)	B _{host} (This work) (μG)
FRB 20110523A	549.6 ^{+12.2} _{-18.1}	–203.7 ± 14.1	–196.2 ± 8.9	–0.46 ± 0.03	–0.44 ± 0.02
FRB 20160102A	2531 ^{+12.1} _{-17.9}	–233.6 ± 10.3	–253.1 ± 9.5	–0.11 ± 0.01	–0.12 ± 0.01
FRB 20181030A	<i>30.4^{+11.7}_{-14.4}</i>	<i>56.2 ± 9.1</i>	<i>60.4 ± 6.3</i>	<i>2.3^{+2.1}_{-0.7}</i>	<i>2.5^{+2.2}_{-0.7}</i>
	<i>30.8^{+11.6}_{-14.5}</i>	<i>57.5 ± 9.2</i>	<i>61.7 ± 6.2</i>	<i>2.3^{+2.2}_{-0.7}</i>	<i>2.5^{+2.2}_{-0.7}</i>
	<i>30.6^{+11.7}_{-14.8}</i>	<i>57.0 ± 9.3</i>	<i>61.5 ± 6.2</i>	<i>2.3^{+2.2}_{-0.7}</i>	<i>2.5^{+2.4}_{-0.7}</i>
FRB 20190117A	314.3 ^{+12.6} _{-18.7}	101.9 ± 9.6	107.3 ± 6.3	0.40 ^{+0.05} _{-0.04}	0.42 ^{+0.04} _{-0.03}
	317.1 ^{+12.8} _{-17.8}	104.2 ± 9.5	109.7 ± 6.4	0.41 ± 0.04	0.43 ^{+0.04} _{-0.03}
FRB 20190213B	218.0 ^{+13.2} _{-18.2}	–13.9 ± 13.7	–26.9 ± 11.8	–0.08 ± 0.08	–0.15 ± 0.07
	218.1 ^{+12.8} _{-17.9}	–9.5 ± 13.5	–22.6 ± 11.7	–0.05 ± 0.08	–0.13 ± 0.07
	218.2 ^{+12.9} _{-18.0}	–9.5 ± 13.6	–22.7 ± 11.6	–0.05 ± 0.08	–0.13 ± 0.07
	218.2 ^{+13.2} _{-18.3}	–9.7 ± 13.7	–22.6 ± 11.7	–0.06 ± 0.08	–0.13 ± 0.07
	218.2 ^{+13.2} _{-17.9}	–10.9 ± 13.6	–23.8 ± 11.6	–0.06 ± 0.08	–0.14 ± 0.07
FRB 20190608B	<i>219.8^{+28.5}_{-55.1}</i>	<i>471.7 ± 17.9</i>	<i>470.4 ± 10.2</i>	<i>2.6^{+0.9}_{-0.3}</i>	<i>2.6^{+0.9}_{-0.3}</i>
FRB 20191108A	505.8 ^{+12.8} _{-18.5}	537.2 ± 14.1	511.2 ± 7.3	1.3 ^{+0.06} _{-0.05}	1.2 ^{+0.05} _{-0.04}
FRB 20200120E	<i>18.9^{+10.1}_{-10.9}</i>	<i>–12.9 ± 7.9</i>	<i>–16.3 ± 6.1</i>	<i>–0.8^{+0.5}_{-1.3}</i>	<i>–1.1^{+0.5}_{-1.5}</i>
	<i>18.8^{+10.3}_{-11.1}</i>	<i>–10.2 ± 8.0</i>	<i>–13.6 ± 6.0</i>	<i>–0.7^{+0.5}_{-1.2}</i>	<i>–0.9^{+0.5}_{-1.3}</i>
	<i>19.0^{+9.9}_{-10.8}</i>	<i>–5.2 ± 15.3</i>	<i>–8.4 ± 14.5</i>	<i>–0.3^{+1.1}_{-1.3}</i>	<i>–0.6^{+1.0}_{-1.4}</i>
	<i>18.8^{+10.4}_{-10.8}</i>	<i>–40.3 ± 9.5</i>	<i>–43.7 ± 7.9</i>	<i>–2.9^{+1.1}_{-3.6}</i>	<i>–2.9^{+1.1}_{-3.9}</i>
	<i>19.1^{+10.1}_{-11.0}</i>	<i>–20.6 ± 9.1</i>	<i>–24.0 ± 7.3</i>	<i>–1.3^{+0.7}_{-1.9}</i>	<i>–1.6^{+0.7}_{-2.1}</i>
	<i>19.1^{+10.1}_{-11.0}</i>	<i>–20.1 ± 11.2</i>	<i>–23.5 ± 10.1</i>	<i>–1.3^{+0.8}_{-2.0}</i>	<i>–1.5^{+0.8}_{-2.2}</i>

[†] DM_{IGM} estimated by Kirsten et al. (2022); we assume no uncertainties on DM_{IGM} in this specific instance.

Sources with TNS names presented in bold face are repeating FRBs. For sources with redshift information, we present the respective rest frame quantity in italics, otherwise the observer frame quantity is provided. All reported uncertainties are the 16th and 84th percentiles except for DM_{MW}, for which they are 20% of the NE2001 prediction (Cordes & Lazio 2002).

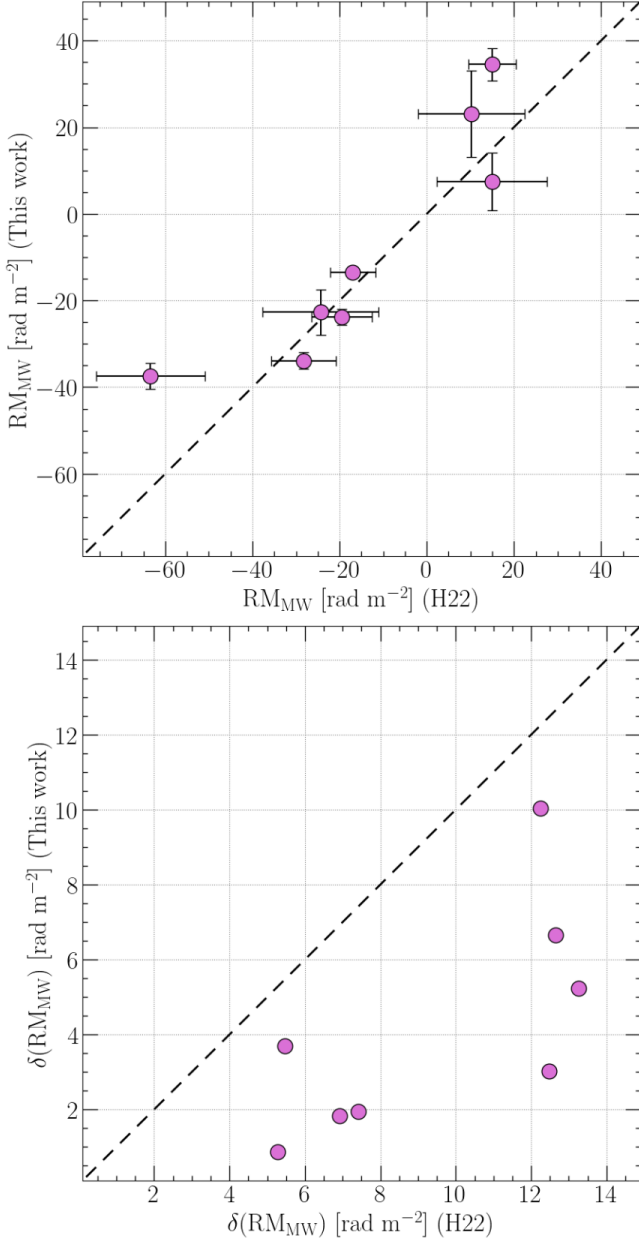


Figure 6. The RM_{MW} (top) and $\delta(\text{RM}_{\text{MW}})$ (bottom) estimates at the position of our eight FRBs between the H22 map and our reconstructed map using VLA RM grids. In both panels, the black dashed line corresponds to unity between the respective estimates.

2023), while at 1.4 GHz it is $6 - 7 \text{ rad m}^{-2}$ (Schnitzeler 2010; Oppermann et al. 2015). The discrepancy between $\sigma(\text{RM}_{\text{EG}})$ estimates at these two frequencies may be due to stronger depolarization effects at lower frequencies. This hypothesis suggests that higher frequency polarization observations should, on average, probe more complex sight-lines (e.g., with more turbulent intrinsic environments or sight-lines passing through turbulent intervening structures). Here, we derive an estimate of

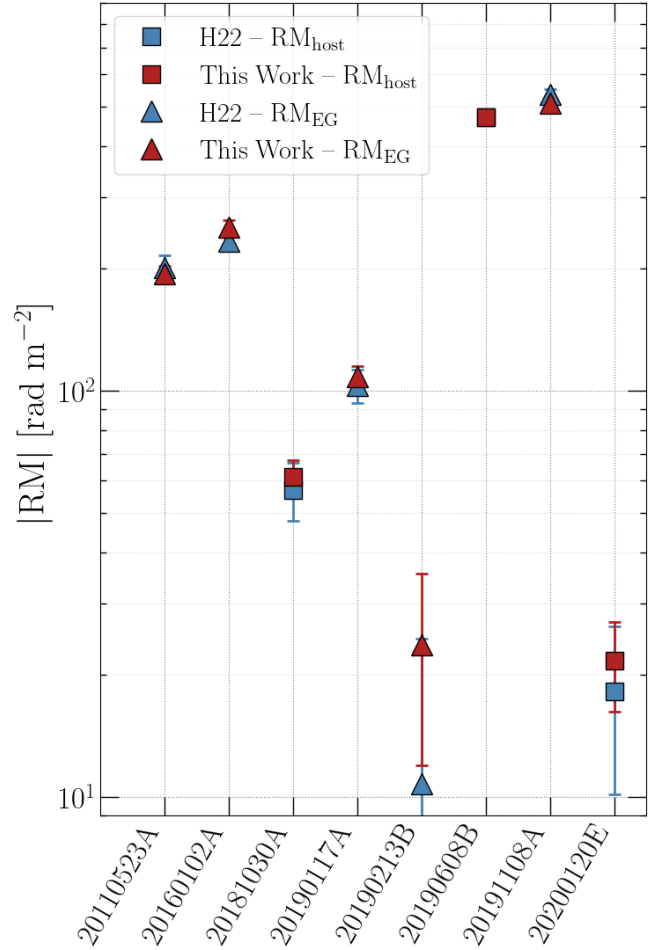


Figure 7. Comparison of the $|\text{RM}_{\text{host}}|$ (squares) or $|\text{RM}_{\text{EG}}|$ (triangles) for all eight FRBs as estimated using the H22 RM_{MW} map (blue) versus the reconstructions from this work (red). The y-axis scaling is logarithmic to highlight the fractional change in $|\text{RM}_{\text{host}}|$.

$\sigma(\text{RM}_{\text{EG}})$ at 3.0 GHz and compare it to the results at lower frequencies to determine if, on average, our higher frequency data probes more complex sight-lines.

To derive an estimate of $\sigma(\text{RM}_{\text{EG}})$ at 3 GHz, we first define a subset of 79 radio galaxies from our combined RM grid data that are Faraday simple ($m_2 < 0.1$) and that have high linearly polarized signal-to-noise ($(\text{S/N})_P > 12$). For each radio galaxy we subtract the Galactic RM towards that position from our RM_{MW} reconstructions and, in Figure 8, we plot the distribution of RM_{EG} for the 79 radio galaxies. We overlay the median RM_{EG} (-0.2 rad m^{-2}) as a solid black line, and the robust standard deviation calculated using the MAD, $\sigma(\text{RM}_{\text{EG,obs}}) = 13.6 \text{ rad m}^{-2}$, is indicated by black dashed lines. Here, we include the subscript “obs” as this estimate still includes the variance introduced by various RM uncertainties. We then obtain $\sigma(\text{RM}_{\text{EG}})$ by

subtracting the variance contributed by the RM measurement uncertainty, $\delta(\text{RM}_{\text{obs}})$, and the statistical error in the RM_{MW} reconstruction, $\delta(\text{RM}_{\text{MW}})$, following Equation 5 of [Osinga et al. \(2024\)](#):

$$\sigma(\text{RM}_{\text{EG}}) = \left(\sigma^2(\text{RM}_{\text{EG,obs}}) - \frac{\sum_i^N (\delta(\text{RM}_{\text{EG}})_i)^2}{N-1} \right)^{1/2}, \quad (17)$$

where $\delta(\text{RM}_{\text{EG}})$ is the quadrature sum of $\delta(\text{RM}_{\text{obs}})$ and $\delta(\text{RM}_{\text{MW}})$, and $N = 79$. Following Equation 17, we derive an estimate of $\sigma(\text{RM}_{\text{EG}}) = 6.8 \text{ rad m}^{-2}$ at 3.0 GHz. To quantify an uncertainty on this estimate, we bootstrap (with replacement) over 10,000 iteration from our $\sigma(\text{RM}_{\text{EG,obs}})$, $\delta(\text{RM}_{\text{obs}})$, and $\delta(\text{RM}_{\text{MW}})$ distributions, and estimate a $\sigma(\text{RM}_{\text{EG}})$ for each iteration. We adopt the standard deviation of the resampled $\sigma(\text{RM}_{\text{EG}})$ distribution as the uncertainty on our estimate, so that $\sigma(\text{RM}_{\text{EG}}) = 6.8 \pm 3.1 \text{ rad m}^{-2}$. We find that our estimate of $\sigma(\text{RM}_{\text{EG}})$ at 3.0 GHz is consistent with those derived at 1.4 GHz by [Schnitzler \(2010\)](#) and [Oppermann et al. \(2015\)](#). We do not find clear frequency dependent variance between $\sigma(\text{RM}_{\text{EG}})$ measurements at 1.4 and 3.0 GHz, but do find that $\sigma(\text{RM}_{\text{EG}})$ as measured at 144 MHz is smaller than our estimate. This suggests that while the much lower frequency observations at 144 MHz are sensitive to depolarization effects and trace LOS that are preferentially less complex, both L-band and S-band observations likely trace similarly complex sight-lines. However, we note that the 144 MHz observations preferentially probe low RM_{obs} sources due to increased intra-channel depolarization at lower observing frequencies and, therefore, may underestimate $\sigma(\text{RM}_{\text{EG}})$. Our $\sigma(\text{RM}_{\text{EG}})$ estimate provides a good reference for future large-sky polarization surveys at > 1.4 GHz, such as VLASS ([Mao et al. 2014](#); [Lacy et al. 2020](#)).

5. DISCUSSION

5.1. FRB magnetoionic environments

By isolating the host galaxy contribution to DM and RM, we can both put constraints on the sources and progenitors of FRBs and identify the subset of FRBs with clean environments that will be the best astrophysical tools for studying intervening media.

We expect different levels of typical $|\text{RM}|$ contributions from different FRB local environments. On the lower density and weakly magnetized end of the spectrum (e.g., globular clusters), we might expect the local environment to contribute $\sim 0 \text{ rad m}^{-2}$. For FRBs in the vicinity of star forming regions in a MW-like galaxy, [Hackstein et al. \(2019\)](#) predict a median $|\text{RM}|$ contribution on the order of 10 rad m^{-2} and up to a few

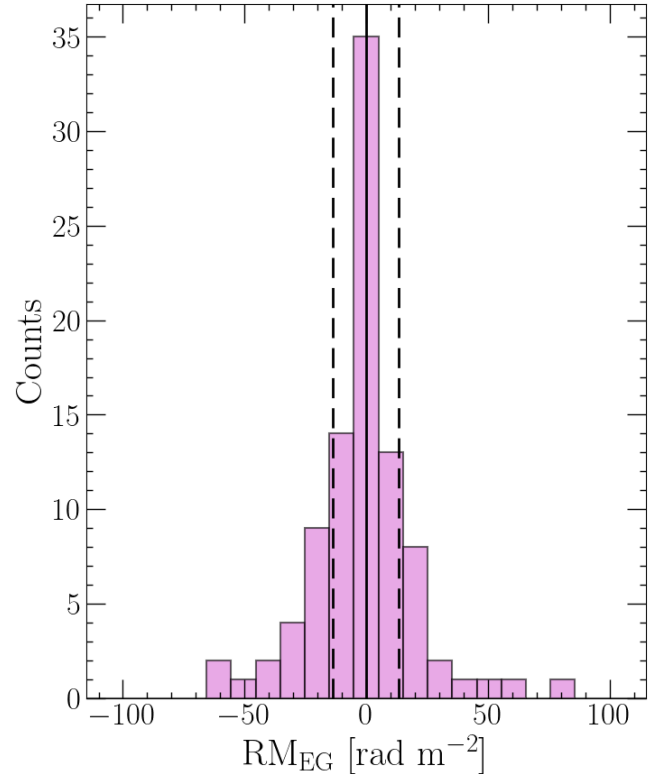


Figure 8. Histogram of the RM_{EG} distribution for the 79 radio galaxies with $m_2 < 0.1$ and $(\text{S/N})_P > 12$. The median is indicated by a black solid line and the robust standard deviation from the MADFM, $\sigma(\text{RM}_{\text{EG,obs}})$, is shown as black dashed lines.

10^2 rad m^{-2} . If instead the FRB is enshrouded by a compact nebula (e.g., a young supernova remnant), we might expect it to contribute up to $\sim 10^3 \text{ rad m}^{-2}$ ([Piro & Gaensler 2018](#)). At high Galactic latitudes ($|b| > 25 \text{ deg}$), we find that the RM_{MW} estimate between H22 and our results changes as little as a few rad m^{-2} to $26 \pm 13 \text{ rad m}^{-2}$. Therefore, our interpretation of the local magnetoionic environment of FRBs with $|\text{RM}_{\text{EG}}| \lesssim 26 \text{ rad m}^{-2}$ (assuming RM_{MW} from H22) can change when using higher density RM grids. Based on the $|\text{RM}_{\text{EG}}|$ distribution of the FRB population studied by [Pandhi et al. \(2024\)](#), which is the largest sample of FRB sources with polarization properties to date, this applies to $\sim 30\%$ of FRBs. Note, however, that $\sim 30\%$ is likely a lower limit, as FRBs at $|b| < 25 \text{ deg}$ will, on average, encounter larger magnitude RM variations over similar or smaller scales.

All eight of our FRBs have RM_{EG} or RM_{host} values that are generally in line with various environments in a MW-like galaxy, [Hackstein et al. \(2019\)](#). Note that those FRBs with RM_{EG} in the observer frame could be at notably larger RM_{host} if the associated host galaxy is at a high redshift. In comparison, the median of

the Galactic pulsar $|\text{RM}|$ distribution is approximately $\sim 70 \text{ rad m}^{-2}$, though the standard deviation is quite large.⁴ The variation observed in our sample of eight FRBs, with $|\text{RM}_{\text{EG}}|$ or $|\text{RM}_{\text{host}}|$ amplitudes spanning $\sim 10 - 500 \text{ rad m}^{-2}$, could imply variety in their local environments (e.g., in the disk versus the halo, or differing vicinity to active sites of star formation and H II regions) or distinct positions within their host galaxies (e.g., smaller or larger offset from the center of the host galaxy or different heights with respect to the host galaxy disk). Two sources in particular, FRB 20190608B ($|\text{RM}_{\text{host}}| = 470.0 \text{ rad m}^{-2}$) and 20191108A ($|\text{RM}_{\text{EG}}| = 511.2 \text{ rad m}^{-2}$) are also consistent with predictions from dense circumburst environments (e.g., within a supernova remnant Piro & Gaensler 2018). Since our sample size is small, we do not draw any conclusions about relative magnetoionic environments of repeaters compared to non-repeaters.

We do not find any significant changes to any of the FRB β or B_{host} estimates after updating the Galactic RM estimate from H22 to our reconstruction. Also, all of our FRBs have β or B_{host} that is generally consistent with the $\sim \mu\text{G}$ level magnetic fields expected in spiral galaxies (Beck 2001). The five FRBs without known redshifts potentially have a significant (unaccounted for) DM_{IGM} contribution, which would cause β to underestimate the rest frame B_{host} by a substantial margin. In addition, the uncertainties in the DM decomposition, particularly for DM_{MW} and DM_{IGM} , are comparatively larger than those in the RM decomposition. Therefore, we find that improving our understanding of the small-scale Galactic RM structure is not the limiting factor for improving estimates of B_{host} for FRBs (for recent examples of studies examining the DM_{host} , RM_{host} , and B_{host} contributed by FRB host galaxies in simulations and observations, see Mo et al. 2023; Mannings et al. 2023; Kovacs et al. 2024; Acharya & Beniamini 2025). Instead, the primary bottlenecks in accurately measuring the FRB host galaxy B_{host} are the lack of redshift information for a large fraction of FRBs and the large uncertainties in DM_{MW} and DM_{IGM} .

In the case of FRB 20190213B, the estimated $|\text{RM}_{\text{EG}}|$ after subtracting the H22 RM_{MW} estimate is 9.5 ± 13.5 to $13.9 \pm 13.7 \text{ rad m}^{-2}$, which is consistent with $|\text{RM}_{\text{EG}}| \sim 0 \text{ rad m}^{-2}$. With our updated RM_{MW} estimate, the $|\text{RM}_{\text{EG}}|$ is now 22.6 ± 11.7 to $26.9 \pm 11.8 \text{ rad m}^{-2}$ and is no longer consistent with $|\text{RM}_{\text{EG}}| \sim 0 \text{ rad m}^{-2}$. Prior to

this work, FRB 20190213B could have been reasonably interpreted as an FRB originating in a clean, weakly magnetized environment, but we have shown that it instead has $|\text{RM}_{\text{EG}}|$ that is similar to what one might expect from some parts of a MW-like host galaxy disk (Hackstein et al. 2019). The case of FRB 20190213B exemplifies how high density RM grids are essential for understanding the magnetoionic environments of low $|\text{RM}_{\text{obs}}|$ FRBs.

Theories of FRB origins often invoke young neutron stars (e.g., Connor et al. 2016; Lyutikov et al. 2016; Metzger et al. 2017, 2019), which are expected to be enshrouded by complex circumburst environments, such as supernova remnants or pulsar/magnetar wind nebulae. In this regard, the population of FRBs with low local environment RM contributions are of particular interest, as they may be located in exceptionally low density circumburst environments. It is possible that this subset of FRBs is associated with an older population of compact objects where the circumburst environment has expanded and dissipated, or where the objects were imparted with a significant velocity kick at birth and have moved away from their birthplace over time. Further, FRBs in weakly magnetized environments are powerful probes of the intergalactic magnetic field strength (Ravi et al. 2016; Akahori et al. 2016) and can help to answer questions about the origins and evolution of cosmic magnetism.

5.2. Prospects with upcoming surveys

The blueprint for reconstructing small-scale Galactic RM fluctuations around FRB positions outlined in this work can be applied directly to any FRB with full Stokes data that falls within the sky coverage of a high source density RM survey. Above a declination of -40 deg , VLASS is expected to provide a catalog of radio galaxy RMs with an average grid density of ~ 7 polarized sources per square degree (Mao et al. 2014). While the density of the RM grids from VLASS will not match those presented in this work, they will still probe angular scales that are a factor of ~ 7 smaller than is currently possible across the northern sky. Prospects in the southern hemisphere are even more promising, with POSSUM cataloging polarized radio galaxies over $20,000 \text{ deg}^2$ below a declination of 0 deg , with a RM grid density of $\sim 30 - 40$ sources per square degree (Vanderwoude et al. 2024; Gaensler et al. 2024). Especially for those FRBs within the latter survey’s footprint, we will be able to accurately isolate local environment RM contributions to FRBs and potentially identify a population of FRBs from low density and weakly magnetized environments

⁴ Based on the 1494 pulsars with RM measurements in the Australia Telescope National Facility pulsar catalog V1.71 (Manchester et al. 2005), which is hosted at <https://www.atnf.csiro.au/research/pulsar/psrcat/>.

that are ideal cosmological probes of intergalactic magnetic fields.

6. CONCLUSIONS

We have conducted two observing campaigns with the Karl G. Jansky Very Large Array to observe the polarization properties of background radio galaxies around eight fast radio burst (FRB) sources at high Galactic latitudes. We apply RM-synthesis on each radio galaxy, deriving RMs and quantifying Faraday complexity in each source that exceeds a linearly polarized signal-to-noise of 8. From the linearly polarized radio sources, we construct RM grids with densities of 9 – 28 sources per square degree around each of the eight target FRBs. We input these RM grids into a Bayesian inference framework, following the steps described by [Khadir et al. \(2024\)](#), to reconstruct continuous maps of the Galactic RM in regions around each FRB sky position. We compare our reconstructed Galactic RM to the current state of the art Galactic RM sky by [Hutschenreuter et al. \(2022\)](#). Finally, we recalculate the RM contributed by the FRB host galaxy and circumburst environment after subtracting our newly computed Galactic RMs towards each FRB. The key conclusions of this work are as follows:

1. In six of the eight fields, we find previously unresolved Galactic RM amplitude variations on angular scales smaller than 1 deg^2 . In five of these fields, we see sharp Galactic RM fluctuations while in one other field we derive a more granular picture of the smooth large-scale RM gradient across the region. We also potentially identify changes in the sign of the RM in two of these fields. Importantly, all of our fields are at high Galactic latitudes ($|b| \geq 25 \text{ deg}$) and we predict that even larger Galactic RM amplitude variations over similar, or smaller, scales are present in regions near the Galactic plane.
2. Towards the FRBs themselves, we see differences of a few rad m^{-2} up to $\sim 40 \text{ rad m}^{-2}$ in the Galactic RM estimate between our results and those of [Hutschenreuter et al. \(2022\)](#). The statistical uncertainties on our Galactic RM estimates also provide a factor of $\sim 2 - 6$ improvement on those by [Hutschenreuter et al. \(2022\)](#). After adjusting the Galactic RM estimate towards FRB 20190213B, we find that its observer frame host galaxy RM is no longer consistent with 0 rad m^{-2} . We suspect that the host galaxy/local environment RM for as much as 30% of all FRB sources (namely those with low observed RM amplitudes) may be

incorrectly interpreted by the currently available, low density RM grids over most of the sky. Since variations in the Galactic RM are expected to be larger in magnitude, and over smaller angular scales, near the Galactic plane, it is possible that 30% is only a lower limit and an even higher fraction of the polarized FRB population is impacted.

With upcoming radio surveys of polarized radio galaxies in the northern (the Very Large Array Sky Survey) and southern (the Polarization Sky Survey of the Universe’s Magnetism) skies, the type of analysis presented in this work will be routinely possible for hundreds to thousands of FRBs, and it will enable us to better understand the progenitors of FRBs from clean magnetoionic environments and identify FRBs that can best probe intergalactic magnetic fields.

ACKNOWLEDGEMENTS

We are grateful to Jamie Farnes, who played a key role in conceiving this project and in obtaining the observations and data. We thank the anonymous reviewer for careful reading of the manuscript and for their constructive feedback. We also thank Shannon Vanderwoude, Amanda Cook, and Erik Osinga for useful feedback on the manuscript. The University of Toronto operates on the traditional land of the Huron-Wendat, the Seneca, and most recently, the Mississaugas of the Credit River; we are grateful to have the opportunity to work on this land. The National Radio Astronomy Observatory and Green Bank Observatory are facilities of the U.S. National Science Foundation operated under cooperative agreement by Associated Universities, Inc. A.P. is funded by the NSERC Canada Graduate Scholarships–Doctoral program. B.M.G. acknowledges the support of the Natural Sciences and Engineering Research Council of Canada (NSERC) through grant RGPIN-2022-03163, and of the Canada Research Chairs program. Z.P. is supported by an NWO Veni fellowship (VI.Veni.222.295). S.P.O. acknowledges support from the Comunidad de Madrid Atracción de Talento program via grant 2022-T1/TIC-23797, and grant PID2023-146372OB-I00 funded by MICIU/AEI/10.13039/501100011033 and by ERDF, EU. Co-funded by the European Union (ERC, ISM-FLOW, 101055318). Views and opinions expressed are, however, those of the author(s) only and do not necessarily reflect those of the European Union or the European Research Council. Neither the European Union nor the granting authority can be held responsible for them. Research at Perimeter Institute is supported in part by the Government of Canada through the Department of Innovation, Science and Economic Development and by the Province

of Ontario through the Ministry of Colleges and Universities.

Facilities: VLA

Software: Astropy (Astropy Collaboration et al. 2013, 2018, 2022), CASA (CASA Team et al. 2022),

Matplotlib (Hunter 2007), NumPy (Harris et al. 2020), PyGEDM (Price et al. 2021), RM-CLEAN (Heald et al. 2009), RM-synthesis (Brentjens & de Bruyn 2005), RM-tools (Purcell et al. 2020), SciPy (Virtanen et al. 2020).

APPENDIX

A. ROTATION MEASURE CATALOG OF POLARIZED RADIO SOURCES

In Table 4, we tabulate the full RM catalog across all eight fields studied in this work. For each linearly polarized radio source, we provide its sky position in degrees, the RM_{obs} with associated measurement uncertainty $\delta(\text{RM}_{\text{obs}})$, the Faraday complexity metric m_2 , and a flag to indicate whether the radio source is Faraday simple (“Y”) or not (“N”). Note that for values of $m_2 < 10^{-2}$, we report $m_2 = 0.00$. The sky positions provided are of the brightest pixel across a given source along which we apply the RM-synthesis analysis and, therefore, does not necessarily correspond to the physical center of the radio galaxy.

Table 4. Rotation measure catalog of all linearly polarized radio sources observed in this work.

J2000 Right Ascension (deg)	J2000 Declination (deg)	RM_{obs} (rad m ⁻²)	$\delta(\text{RM}_{\text{obs}})$ (rad m ⁻²)	m_2	Faraday simple?
Field: FRB 20110523A					
326.952	-0.491	29.9	7.3	0.00	Y
327.030	-0.815	51	12	0.00	Y
326.171	0.450	10.4	3.9	0.00	Y
326.263	0.535	13.7	4.2	0.00	Y
325.970	-0.142	9.3	5.5	0.00	Y
325.970	-0.466	-26.2	7.3	0.00	Y
325.665	-0.904	21	12	0.00	Y
Field: FRB 20160102A					
339.285	-30.346	24.4	2.7	0.00	Y
339.286	-30.342	23.4	1.3	0.15	N
339.310	-30.088	39	13	0.00	Y
339.362	-30.190	18.7	5.3	0.00	Y
339.420	-29.849	-2.8	6.4	0.00	Y
339.525	-30.100	36.1	8.5	0.00	Y
339.589	-30.346	-39	14	0.00	Y
339.678	-30.114	41.5	3.0	0.00	Y
339.771	-29.707	23.0	4.7	0.00	Y
339.794	-30.616	11.9	3.4	0.00	Y
339.797	-30.619	23	12	0.00	Y
339.894	-30.072	40.6	8.3	0.00	Y
339.988	-30.378	18.58	0.86	0.00	Y
339.987	-30.380	34.5	1.7	0.00	Y
340.078	-30.365	40.7	6.7	0.00	Y
Field: FRB 20181030A					
157.525	73.424	786	12	0.00	Y
157.640	73.978	-26	11	0.00	Y

Continued on next page

Table 4 – continued from previous page

J2000 Right Ascension (deg)	J2000 Declination (deg)	RM_{obs} (rad m ⁻²)	$\delta(RM_{\text{obs}})$ (rad m ⁻²)	m_2	Faraday simple?
157.969	73.426	-28	24	0.10	N
158.006	73.429	-21	23	0.10	N
158.073	74.063	-55	71	0.23	N
159.217	73.655	-13.5	8.7	0.00	Y
159.904	73.429	-30	59	0.24	N
160.243	73.919	1.9	8.4	0.00	Y
Field: FRB 20190117A					
331.275	17.125	54	10	0.00	Y
331.312	17.181	5.6	8.9	0.00	Y
331.444	17.210	-39.7	5.4	0.00	Y
331.447	17.210	-33	12	0.00	Y
331.713	17.172	-37.4	6.3	0.00	Y
331.744	17.159	-33.8	2.6	0.00	Y
331.782	17.374	-51.4	4.1	0.00	Y
331.783	17.374	-54	52	0.22	N
331.849	17.596	-34.5	2.7	0.00	Y
331.958	17.208	-69.9	9.3	0.00	Y
332.051	17.564	-48.3	2.8	0.00	Y
332.055	17.564	-20	37	0.16	N
332.084	17.549	-34	13	0.00	Y
332.163	17.354	-39.8	2.6	0.00	Y
331.956	17.204	-78	12	0.00	Y
331.706	17.173	-59	13	0.00	Y
Field: FRB 20190213B					
274.102	81.477	12.2	3.8	0.00	Y
274.580	81.422	-18.0	7.7	0.00	Y
275.879	81.806	44.2	1.1	0.09	Y
275.899	81.810	52.2	5.3	0.00	Y
275.919	81.415	9.3	5.4	0.00	Y
275.956	81.414	22.9	2.5	0.00	Y
276.043	81.229	-2.5	8.0	0.00	Y
276.255	81.740	36	11	0.00	Y
276.412	81.306	-394	54	0.24	N
277.431	81.341	3	37	0.16	N
277.562	80.987	20.3	7.5	0.00	Y
277.576	80.998	0.5	7.3	0.00	Y
Field: FRB 20190608B					
333.589	-8.053	3	10	0.00	Y
333.601	-8.083	-46.1	7.8	0.00	Y
333.644	-8.084	-36	31	0.13	N
333.869	-8.329	-13.27	0.71	0.00	Y
333.955	-7.960	0.7	8.0	0.00	Y
333.956	-7.961	-30.4	4.0	0.00	Y
334.038	-8.276	-24.3	2.9	0.00	Y
334.042	-8.278	-31	43	0.19	N
334.051	-7.875	-21	29	0.12	N

Continued on next page

Table 4 – continued from previous page

J2000 Right Ascension (deg)	J2000 Declination (deg)	RM_{obs} (rad m^{-2})	$\delta(RM_{\text{obs}})$ (rad m^{-2})	m_2	Faraday simple?
334.081	-8.252	-11.4	8.4	0.00	Y
Field: FRB 20191108A					
22.908	31.793	-82	12	0.00	Y
23.011	31.947	-67	11	0.00	Y
23.011	31.948	-86	47	0.20	N
23.037	31.949	-64.1	7.8	0.00	Y
23.322	31.874	-41.7	6.0	0.00	Y
23.492	31.721	-33.2	3.1	0.00	Y
23.522	32.074	-96	12	0.00	Y
23.669	32.079	-31.7	8.6	0.00	Y
22.904	31.790	-49	12	0.00	Y
Field: FRB 20200120E					
148.300	69.068	-55	33	0.14	N
148.550	68.982	-43.1	5.1	0.00	Y
148.888	69.065	-22.9	2.1	0.00	Y
149.091	68.766	-4.4	7.2	0.00	Y
149.095	68.767	-53.6	4.6	0.00	Y
149.426	68.742	2	68	0.24	N
149.450	69.175	-32	71	0.21	N
149.452	69.180	-13.3	1.5	0.05	Y
149.745	68.768	-14.3	5.2	0.00	Y
149.749	68.539	-19.8	1.6	0.00	Y
149.774	68.548	-31.0	1.7	0.00	Y
149.829	68.567	-7.5	5.9	0.00	Y
149.832	68.563	50	91	0.23	N
150.002	68.523	31.0	6.9	0.20	N
150.038	68.537	-8	50	0.22	N
150.072	68.652	-1308	14	0.00	Y
150.276	68.835	-8.7	2.0	0.07	Y
150.285	68.834	-5.0	1.2	0.08	Y
150.537	68.978	-628	38	0.19	N
150.537	68.977	-330	43	0.18	N
150.609	68.973	-53.5	3.0	0.00	Y
150.615	68.975	-4.0	1.5	0.00	Y

REFERENCES

- Acharya, S. K., & Beniamini, P. 2025, JCAP, 2025, 036, doi: [10.1088/1475-7516/2025/01/036](https://doi.org/10.1088/1475-7516/2025/01/036)
- Akahori, T., Ryu, D., & Gaensler, B. M. 2016, ApJ, 824, 105, doi: [10.3847/0004-637X/824/2/105](https://doi.org/10.3847/0004-637X/824/2/105)
- Astropy Collaboration, Robitaille, T. P., Tollerud, E. J., et al. 2013, A&A, 558, A33, doi: [10.1051/0004-6361/201322068](https://doi.org/10.1051/0004-6361/201322068)
- Astropy Collaboration, Price-Whelan, A. M., Sipőcz, B. M., et al. 2018, AJ, 156, 123, doi: [10.3847/1538-3881/aabc4f](https://doi.org/10.3847/1538-3881/aabc4f)
- Astropy Collaboration, Price-Whelan, A. M., Lim, P. L., et al. 2022, ApJ, 935, 167, doi: [10.3847/1538-4357/ac7c74](https://doi.org/10.3847/1538-4357/ac7c74)
- Bannister, K. W., Deller, A. T., Phillips, C., et al. 2019, Science, 365, 565, doi: [10.1126/science.aaw5903](https://doi.org/10.1126/science.aaw5903)

- Baptista, J., Prochaska, J. X., Mannings, A. G., et al. 2024, *ApJ*, 965, 57, doi: [10.3847/1538-4357/ad2705](https://doi.org/10.3847/1538-4357/ad2705)
- Beck, R. 2001, *SSRv*, 99, 243, doi: [10.1023/A:1013805401252](https://doi.org/10.1023/A:1013805401252)
- Bhandari, S., Keane, E. F., Barr, E. D., et al. 2018, *MNRAS*, 475, 1427, doi: [10.1093/mnras/stx3074](https://doi.org/10.1093/mnras/stx3074)
- Bhandari, S., Sadler, E. M., Prochaska, J. X., et al. 2020a, *ApJL*, 895, L37, doi: [10.3847/2041-8213/ab672e](https://doi.org/10.3847/2041-8213/ab672e)
- Bhandari, S., Bannister, K. W., Lenc, E., et al. 2020b, *ApJL*, 901, L20, doi: [10.3847/2041-8213/abb462](https://doi.org/10.3847/2041-8213/abb462)
- Bhardwaj, M., Kirichenko, A. Y., Michilli, D., et al. 2021a, *ApJL*, 919, L24, doi: [10.3847/2041-8213/ac223b](https://doi.org/10.3847/2041-8213/ac223b)
- Bhardwaj, M., Gaensler, B. M., Kaspi, V. M., et al. 2021b, *ApJL*, 910, L18, doi: [10.3847/2041-8213/abeaa6](https://doi.org/10.3847/2041-8213/abeaa6)
- Bhardwaj, M., Michilli, D., Kirichenko, A. Y., et al. 2024, *ApJL*, 971, L51, doi: [10.3847/2041-8213/ad64d1](https://doi.org/10.3847/2041-8213/ad64d1)
- Brentjens, M. A., & de Bruyn, A. G. 2005, *A&A*, 441, 1217, doi: [10.1051/0004-6361:20052990](https://doi.org/10.1051/0004-6361:20052990)
- Briggs, D. S. 1995, PhD thesis, New Mexico Institute of Mining and Technology
- Brown, S. 2011, Internal POSSUM Report #9: Assess the Complexity of an RM Synthesis Spectrum. https://askap.org/possum/wiki/uploads/Documents/possumreport_009.pdf
- Burn, B. J. 1966, *MNRAS*, 133, 67, doi: [10.1093/mnras/133.1.67](https://doi.org/10.1093/mnras/133.1.67)
- Caleb, M., Keane, E. F., van Straten, W., et al. 2018, *MNRAS*, 478, 2046, doi: [10.1093/mnras/sty1137](https://doi.org/10.1093/mnras/sty1137)
- CASA Team, Bean, B., Bhatnagar, S., et al. 2022, *PASP*, 134, 114501, doi: [10.1088/1538-3873/ac9642](https://doi.org/10.1088/1538-3873/ac9642)
- Chatterjee, S., Law, C. J., Wharton, R. S., et al. 2017, *Nature*, 541, 58, doi: [10.1038/nature20797](https://doi.org/10.1038/nature20797)
- CHIME/FRB Collaboration, Amiri, M., Andersen, B. C., et al. 2021, *ApJS*, 257, 59, doi: [10.3847/1538-4365/ac33ab](https://doi.org/10.3847/1538-4365/ac33ab)
- . 2024, *ApJ*, 969, 145, doi: [10.3847/1538-4357/ad464b](https://doi.org/10.3847/1538-4357/ad464b)
- Chittidi, J. S., Simha, S., Mannings, A., et al. 2021, *ApJ*, 922, 173, doi: [10.3847/1538-4357/ac2818](https://doi.org/10.3847/1538-4357/ac2818)
- Condon, J. J., Cotton, W. D., Greisen, E. W., et al. 1998, *AJ*, 115, 1693, doi: [10.1086/300337](https://doi.org/10.1086/300337)
- Connor, L., Sievers, J., & Pen, U.-L. 2016, *MNRAS*, 458, L19, doi: [10.1093/mnrasl/slv124](https://doi.org/10.1093/mnrasl/slv124)
- Connor, L., van Leeuwen, J., Oostrum, L. C., et al. 2020, *MNRAS*, 499, 4716, doi: [10.1093/mnras/staa3009](https://doi.org/10.1093/mnras/staa3009)
- Cook, A. M., Bhardwaj, M., Gaensler, B. M., et al. 2023, *ApJ*, 946, 58, doi: [10.3847/1538-4357/acbbd0](https://doi.org/10.3847/1538-4357/acbbd0)
- Cordes, J. M., & Lazio, T. J. W. 2002, arXiv e-prints, astro, doi: [10.48550/arXiv.astro-ph/0207156](https://doi.org/10.48550/arXiv.astro-ph/0207156)
- Day, C. K., Deller, A. T., Shannon, R. M., et al. 2020, *MNRAS*, 497, 3335, doi: [10.1093/mnras/staa2138](https://doi.org/10.1093/mnras/staa2138)
- Dolag, K., Gaensler, B. M., Beck, A. M., & Beck, M. C. 2015, *MNRAS*, 451, 4277, doi: [10.1093/mnras/stv1190](https://doi.org/10.1093/mnras/stv1190)
- Edenhofer, G., Frank, P., Roth, J., et al. 2024, *Journal of Open Source Software*, 9, 6593, doi: [10.21105/joss.06593](https://doi.org/10.21105/joss.06593)
- Gaensler, B., et al. 2024, *PASA*, submitted
- Gordon, Y. A., Boyce, M. M., O’Dea, C. P., et al. 2021, *ApJS*, 255, 30, doi: [10.3847/1538-4365/ac05c0](https://doi.org/10.3847/1538-4365/ac05c0)
- Hackstein, S., Brüggem, M., Vazza, F., Gaensler, B. M., & Heesen, V. 2019, *MNRAS*, 488, 4220, doi: [10.1093/mnras/stz2033](https://doi.org/10.1093/mnras/stz2033)
- Harris, C. R., Millman, K. J., van der Walt, S. J., et al. 2020, *Nature*, 585, 357, doi: [10.1038/s41586-020-2649-2](https://doi.org/10.1038/s41586-020-2649-2)
- Heald, G., Braun, R., & Edmonds, R. 2009, *A&A*, 503, 409, doi: [10.1051/0004-6361/200912240](https://doi.org/10.1051/0004-6361/200912240)
- Högbom, J. A. 1974, *A&AS*, 15, 417
- Hunter, J. D. 2007, *Computing in Science & Engineering*, 9, 90, doi: [10.1109/MCSE.2007.55](https://doi.org/10.1109/MCSE.2007.55)
- Hutschenreuter, S., & Enßlin, T. A. 2020, *A&A*, 633, A150, doi: [10.1051/0004-6361/201935479](https://doi.org/10.1051/0004-6361/201935479)
- Hutschenreuter, S., Haverkorn, M., Frank, P., Raycheva, N. C., & Enßlin, T. A. 2024, *A&A*, 690, A314, doi: [10.1051/0004-6361/202346740](https://doi.org/10.1051/0004-6361/202346740)
- Hutschenreuter, S., Anderson, C. S., Betti, S., et al. 2022, *A&A*, 657, A43, doi: [10.1051/0004-6361/202140486](https://doi.org/10.1051/0004-6361/202140486)
- Khadir, A., Pandhi, A., Hutschenreuter, S., et al. 2024, arXiv e-prints, arXiv:2410.15265, doi: [10.48550/arXiv.2410.15265](https://doi.org/10.48550/arXiv.2410.15265)
- Kirsten, F., Marcote, B., Nimmo, K., et al. 2022, *Nature*, 602, 585, doi: [10.1038/s41586-021-04354-w](https://doi.org/10.1038/s41586-021-04354-w)
- Kovacs, T. O., Mao, S. A., Basu, A., et al. 2024, *A&A*, 690, A47, doi: [10.1051/0004-6361/202347459](https://doi.org/10.1051/0004-6361/202347459)
- Lacy, M., Baum, S. A., Chandler, C. J., et al. 2020, *PASP*, 132, 035001, doi: [10.1088/1538-3873/ab63eb](https://doi.org/10.1088/1538-3873/ab63eb)
- Lam, M. T., Cordes, J. M., Chatterjee, S., et al. 2016, *ApJ*, 821, 66, doi: [10.3847/0004-637X/821/1/66](https://doi.org/10.3847/0004-637X/821/1/66)
- Law, C. J., Sharma, K., Ravi, V., et al. 2024, *ApJ*, 967, 29, doi: [10.3847/1538-4357/ad3736](https://doi.org/10.3847/1538-4357/ad3736)
- Lorimer, D. R., Bailes, M., McLaughlin, M. A., Narkevic, D. J., & Crawford, F. 2007, *Science*, 318, 777, doi: [10.1126/science.1147532](https://doi.org/10.1126/science.1147532)
- Lyutikov, M., Burzawa, L., & Popov, S. B. 2016, *MNRAS*, 462, 941, doi: [10.1093/mnras/stw1669](https://doi.org/10.1093/mnras/stw1669)
- Ma, Y. K., Mao, S. A., Stil, J., et al. 2019, *MNRAS*, 487, 3454, doi: [10.1093/mnras/stz1328](https://doi.org/10.1093/mnras/stz1328)
- Macquart, J. P., Ekers, R. D., Feain, I., & Johnston-Hollitt, M. 2012, *ApJ*, 750, 139, doi: [10.1088/0004-637X/750/2/139](https://doi.org/10.1088/0004-637X/750/2/139)
- Macquart, J. P., Prochaska, J. X., McQuinn, M., et al. 2020, *Nature*, 581, 391, doi: [10.1038/s41586-020-2300-2](https://doi.org/10.1038/s41586-020-2300-2)

- Manchester, R. N., Hobbs, G. B., Teoh, A., & Hobbs, M. 2005, *AJ*, 129, 1993, doi: [10.1086/428488](https://doi.org/10.1086/428488)
- Mannings, A. G., Pakmor, R., Prochaska, J. X., et al. 2023, *ApJ*, 954, 179, doi: [10.3847/1538-4357/ace7bb](https://doi.org/10.3847/1538-4357/ace7bb)
- Mao, S. A., Banfield, J., Gaensler, B., et al. 2014, arXiv e-prints, arXiv:1401.1875, doi: [10.48550/arXiv.1401.1875](https://doi.org/10.48550/arXiv.1401.1875)
- Marcote, B., Nimmo, K., Hessels, J. W. T., et al. 2020, *Nature*, 577, 190, doi: [10.1038/s41586-019-1866-z](https://doi.org/10.1038/s41586-019-1866-z)
- Masui, K., Lin, H.-H., Sievers, J., et al. 2015, *Nature*, 528, 523, doi: [10.1038/nature15769](https://doi.org/10.1038/nature15769)
- Mckinven, R., Gaensler, B. M., Michilli, D., et al. 2023, *ApJ*, 951, 82, doi: [10.3847/1538-4357/acd188](https://doi.org/10.3847/1538-4357/acd188)
- Metzger, B. D., Berger, E., & Margalit, B. 2017, *ApJ*, 841, 14, doi: [10.3847/1538-4357/aa633d](https://doi.org/10.3847/1538-4357/aa633d)
- Metzger, B. D., Margalit, B., & Sironi, L. 2019, *MNRAS*, 485, 4091, doi: [10.1093/mnras/stz700](https://doi.org/10.1093/mnras/stz700)
- Mevius, M. 2018, *ASCL*. <https://ascl.net/1806.024>
- Michilli, D., Bhardwaj, M., Brar, C., et al. 2023, *ApJ*, 950, 134, doi: [10.3847/1538-4357/accf89](https://doi.org/10.3847/1538-4357/accf89)
- Mo, J.-F., Zhu, W., Wang, Y., Tang, L., & Feng, L.-L. 2023, *MNRAS*, 518, 539, doi: [10.1093/mnras/stac3104](https://doi.org/10.1093/mnras/stac3104)
- Ng, C., Pandhi, A., Mckinven, R., et al. 2024, arXiv e-prints, arXiv:2411.09045, doi: [10.48550/arXiv.2411.09045](https://doi.org/10.48550/arXiv.2411.09045)
- Nimmo, K., Hessels, J. W. T., Kirsten, F., et al. 2022, *Nature Astronomy*, 6, 393, doi: [10.1038/s41550-021-01569-9](https://doi.org/10.1038/s41550-021-01569-9)
- Niu, C. H., Aggarwal, K., Li, D., et al. 2022, *Nature*, 606, 873, doi: [10.1038/s41586-022-04755-5](https://doi.org/10.1038/s41586-022-04755-5)
- Oppermann, N., Junklewitz, H., Robbers, G., et al. 2012, *A&A*, 542, A93, doi: [10.1051/0004-6361/201118526](https://doi.org/10.1051/0004-6361/201118526)
- Oppermann, N., Junklewitz, H., Greiner, M., et al. 2015, *A&A*, 575, A118, doi: [10.1051/0004-6361/201423995](https://doi.org/10.1051/0004-6361/201423995)
- Osinga, E., van Weeren, R. J., Rudnick, L., et al. 2024, arXiv e-prints, arXiv:2408.07178, doi: [10.48550/arXiv.2408.07178](https://doi.org/10.48550/arXiv.2408.07178)
- O'Sullivan, S. P., Shimwell, T. W., Hardcastle, M. J., et al. 2023, *MNRAS*, 519, 5723, doi: [10.1093/mnras/stac3820](https://doi.org/10.1093/mnras/stac3820)
- Pandhi, A., Hutschenreuter, S., West, J. L., Gaensler, B. M., & Stock, A. 2022, *MNRAS*, 516, 4739, doi: [10.1093/mnras/stac2314](https://doi.org/10.1093/mnras/stac2314)
- Pandhi, A., Pleunis, Z., Mckinven, R., et al. 2024, *ApJ*, 968, 50, doi: [10.3847/1538-4357/ad40aa](https://doi.org/10.3847/1538-4357/ad40aa)
- Piro, A. L., & Gaensler, B. M. 2018, *ApJ*, 861, 150, doi: [10.3847/1538-4357/aac9bc](https://doi.org/10.3847/1538-4357/aac9bc)
- Price, D. C., Flynn, C., & Deller, A. 2021, *PASA*, 38, e038, doi: [10.1017/pasa.2021.33](https://doi.org/10.1017/pasa.2021.33)
- Purcell, C. R., Van Eck, C. L., West, J., Sun, X. H., & Gaensler, B. M. 2020, *ASCL*, 2005.003. <http://ascl.net/2005.003>
- Ravi, V., Shannon, R. M., Bailes, M., et al. 2016, *Science*, 354, 1249, doi: [10.1126/science.aaf6807](https://doi.org/10.1126/science.aaf6807)
- Schnitzeler, D. H. F. M. 2010, *MNRAS*, 409, L99, doi: [10.1111/j.1745-3933.2010.00957.x](https://doi.org/10.1111/j.1745-3933.2010.00957.x)
- Shannon, R. M., Bannister, K. W., Bera, A., et al. 2024, arXiv e-prints, arXiv:2408.02083, doi: [10.48550/arXiv.2408.02083](https://doi.org/10.48550/arXiv.2408.02083)
- Sharma, K., Ravi, V., Connor, L., et al. 2024, *Nature*, 635, 61, doi: [10.1038/s41586-024-08074-9](https://doi.org/10.1038/s41586-024-08074-9)
- Sherman, M. B., Connor, L., Ravi, V., et al. 2024, *ApJ*, 964, 131, doi: [10.3847/1538-4357/ad275e](https://doi.org/10.3847/1538-4357/ad275e)
- Sobey, C., Bilous, A. V., Griefmeier, J. M., et al. 2019, *MNRAS*, 484, 3646, doi: [10.1093/mnras/stz214](https://doi.org/10.1093/mnras/stz214)
- Taylor, A. R., Stil, J. M., & Sunstrum, C. 2009, *ApJ*, 702, 1230, doi: [10.1088/0004-637X/702/2/1230](https://doi.org/10.1088/0004-637X/702/2/1230)
- Thomson, A. J. M., McConnell, D., Lenc, E., et al. 2023, *PASA*, 40, e040, doi: [10.1017/pasa.2023.38](https://doi.org/10.1017/pasa.2023.38)
- Van Eck, C. L., Gaensler, B. M., Hutschenreuter, S., et al. 2023, *ApJS*, 267, 28, doi: [10.3847/1538-4365/acda24](https://doi.org/10.3847/1538-4365/acda24)
- Vanderwoude, S., West, J. L., Gaensler, B. M., et al. 2024, *AJ*, 167, 226, doi: [10.3847/1538-3881/ad2fc8](https://doi.org/10.3847/1538-3881/ad2fc8)
- Virtanen, P., Gommers, R., Oliphant, T. E., et al. 2020, *Nature Methods*, 17, 261, doi: [10.1038/s41592-019-0686-2](https://doi.org/10.1038/s41592-019-0686-2)
- Yamasaki, S., & Totani, T. 2020, *ApJ*, 888, 105, doi: [10.3847/1538-4357/ab58c4](https://doi.org/10.3847/1538-4357/ab58c4)